3-4-2014

The Impact of Slab Dip Variations, Gaps and Rollback on Mantle Wedge Flow: Insights from Fluids Experiments

Julia G. MacDougall

Chris Kincaid
University of Rhode Island, kincaid@uri.edu

Sara Szwaja

Karen M. Fischer

Follow this and additional works at: https://digitalcommons.uri.edu/gsofacpubs

The Impact of Slab Dip Variations, Gaps and Rollback on Mantle Wedge Flow: Insights from Fluids Experiments

Publisher Statement

Terms of Use

The impact of slab dip variations, gaps and rollback on mantle wedge flow: insights from fluids experiments

Julia G. MacDougall,[1] Chris Kincaid,[2] Sara Szwaja[2] and Karen M. Fischer[1]

[1]*Department of Geological Sciences, Brown University, Providence, RI 02912, USA. E-mail: julia_macdougall@brown.edu*
[2]*Graduate School of Oceanography, University of Rhode Island, Narragansett, RI 02882, USA*

SUMMARY

Observed seismic anisotropy and geochemical anomalies indicate the presence of 3-D flow around and above subducting slabs. To investigate how slab geometry and velocity affect mantle flow, we conducted a set of experiments using a subduction apparatus in a fluid-filled tank. Our models comprise two independently adjustable, continuous belts to represent discrete sections of subducting slabs that kinematically drive flow in the surrounding glucose syrup that represents the upper mantle. We analyse how slab dip (ranging from $30°$ to $80°$), slab dip difference between slab segments (ranging from $20°$ to $50°$), rates of subduction (4–8 cm yr^{-1}) and slab/trench rollback (0–3 cm yr^{-1}) affect mantle flow. Whiskers were used to approximate mineral alignment induced by the flow, as well as to predict directions of seismic anisotropy. We find that dip variations between slab segments generate 3-D flow in the mantle wedge, where the path lines of trenchward moving mantle material above the slab are deflected towards the slab segment with the shallower dip. The degree of path line deflection increases as the difference in slab dip between the segments increases, and, for a fixed dip difference, as slab dip decreases. In cases of slab rollback and large slab dip differences, we observe intrusion of subslab material through the gap and into the wedge. Flow through the gap remains largely horizontal before eventual downward entrainment. Whisker alignment in the wedge flow is largely trench-normal, except near the lateral edges of the slab where toroidal flow dominates. In addition, whisker azimuths located above the slab gap deviate most strongly from trench-normal orientations when slab rollback does not occur. Such flow field complexities are likely sufficient to affect deep melt production and shallow melt delivery. However, none of the experiments produced flow fields that explain the trench-parallel shear wave splitting fast directions observed over broad arc and backarc regions in many subduction zones.

Key words: Seismic anisotropy; Subduction zone processes; Dynamics of lithosphere and mantle.

INTRODUCTION

Subduction drives plate tectonics and greatly influences mantle flow patterns and melt pathways between the mantle wedge and volcanic arcs. The results of previous geological, geophysical and geodynamic studies have provided essential insight on subduction zone mantle flow. Early analytical (Tovish *et al.* 1978) and numerical models of subduction defined a mode of plate-induced, 2-D corner flow in the mantle wedge, including trench-normal flow of material towards the trench and its subsequent entrainment with the subducting slab (e.g. Davies 1977; Garfunkel *et al.* 1986; Ribe 1989a). This style of 2-D modelling has revealed important relationships between subduction parameters and slab thermal evolution (Peacock 1996; Kincaid & Sacks 1997; van Keken *et al.* 2002; Peacock 2003; Syracuse *et al.* 2010). Additional 2-D cases consider how corner flow patterns, temperatures and melt production in the mantle wedge are influenced by slab rollback (Garfunkel *et al.* 1986), backarc extension (Ribe 1989a; Conder *et al.* 2002; Kincaid & Hall 2003), non-Newtonian rheology (van Keken *et al.* 2002; Kelemen *et al.* 2003) and viscosity anisotropy (Lev & Hager 2011). 2-D models have also been used to define a type of secondary convection in which buoyant diapirs (for example, partially molten hydrated mantle and/or hydrated mantle plus slab crust and sediment rising off of the subducting slab) interact with plate-scale flows within the mantle wedge (e.g. Gerya & Yuen 2003; Gerya *et al.* 2004).

Other geochemical, seismic and geodynamic studies have emphasized the 3-D nature of subduction zone flow and related processes. Geochemical data indicate 3-D circulation of distinct mantle material with anomalous compositions around slab edges or through slab gaps (Klein & Karsten 1995; Karsten *et al.* 1996;

Turner & Hawkesworth 1998; Faccenna *et al.* 2005; Falloon *et al.* 2007; Regelous *et al.* 2008; Gazel *et al.* 2011). A number of observational studies call for entrainment of Samoan plume material along a trench-parallel trajectory from the north to interact with the Tonga subduction zone and the Lau backarc spreading centre (Wendt *et al.* 1997; Turner & Hawkesworth 1998; Hart *et al.* 2004). Similarly, geochemical models for the Central American subduction zone invoke the opening of a slab window (Abratis & Worner 2001), toroidal flow around the retreating Nazca Plate and into the wedge (Herrstrom *et al.* 1995) and complex entrainment of Galapagos plume material into the forearc beneath Central American arc volcanoes (Gazel *et al.* 2011). Spatial–temporal trends in arc geochemical anomalies have also been used to argue for trench-parallel transport in the mantle wedge (Hoernle *et al.* 2008; Regelous *et al.* 2008; Escrig *et al.* 2009).

Seismological constraints on anisotropy in subduction zones also indicate mantle deformation consistent with 3-D flow. B-type olivine fabrics (Jung & Karato 2001; Jung *et al.* 2006; Lassak *et al.* 2006; Karato *et al.* 2008; Long 2013; Faccenda and Capitanio 2013) and serpentine fabrics (e.g. Katayama *et al.* 2009; Jung 2011) may exist in the cold corner of the mantle wedge (Kneller *et al.* 2005; Kneller *et al.* 2007), and anisotropy in the slab may be influential on certain paths near the trench (Healy *et al.* 2009; Hammond *et al.* 2010). However, outside of these regions, shear wave splitting observations, including trench-parallel fast polarizations, provide evidence for 3-D flow in the mantle wedge (Yang *et al.* 1995; Fouch & Fischer 1996; Audoine *et al.* 2000; Smith *et al.* 2001; Levin *et al.* 2004; Long & van der Hilst 2006; Hoernle *et al.* 2008; Long & Silver 2008; Abt *et al.* 2009; MacDougall *et al.* 2012; Long 2013), the subslab mantle (Russo & Silver 1994; Fouch & Fischer 1996; Audoine *et al.* 2000; Matcham *et al.* 2000; Anderson *et al.* 2004; Civello & Margheriti 2004; Baccheschi *et al.* 2007; Long & Silver 2008; Abt *et al.* 2010; Christensen & Abers 2010; Hicks *et al.* 2012; MacDougall *et al.* 2012; Long 2013), as well as flow through slab gaps (e.g. Russo *et al.* 2010) and around slab edges (e.g. Peyton *et al.* 2001).

While 2-D models have proven valuable, numerous geodynamic studies have also shown that mantle flow above, below and around subducting slabs is fundamentally 3-D, thus motivating our experiments with 3-D flow driven by kinematic subduction. Models representing dynamic subduction of discrete slab segments show that rollback occurs naturally and produces a strong toroidal flow of subslab mantle around the slab edges and into the mantle wedge (Kincaid & Olson 1987; Funiciello *et al.* 2003; Schellart 2004; Funiciello *et al.* 2006; Piromallo *et al.* 2006; Honda 2008, 2009; Billen & Jadamec 2012; Faccenda & Capitanio 2012, 2013). The length scales of toroidal and poloidal flow are positively correlated with slab width (Schellart 2004; Funiciello *et al.* 2006; Piromallo *et al.* 2006; Becker & Faccenna 2009; Li & Ribe 2012; Faccenda & Capitanio 2013) and slab viscosity (Piromallo *et al.* 2006; Billen & Jadamec 2012; Jadamec & Billen 2012). Varying dip values and rollback rates can cause time-variable mantle flow patterns both above and below the slab (Kincaid & Griffiths 2004). These flow patterns control the spatial and temporal development of anisotropic fabrics in the wedge (e.g. Buttles & Olson 1998; Druken *et al.* 2011), a fact that we exploit in our experiments in an effort to understand the origin of anisotropy with a trench-parallel fast direction in the mantle wedge.

3-D kinematic models suggest that rollback-induced mantle flow fields deform and stall thermally buoyant upwellings, effectively converting these density and viscosity anomalies into passive features embedded within large-scale, plate-driven circulation (Druken

et al. 2013; Kincaid *et al.* 2013). These models have also shown that changes in subduction style, from downdip-only motion to rollback sinking, can produce strong variations in slab thermal evolution, buoyant upwelling rates and temperatures throughout the wedge (Kincaid & Griffiths 2003, 2004; Kincaid *et al.* 2013). In addition, 3-D slab morphologies yield significantly 3-D local flow patterns (Kneller & van Keken 2007, 2008; Jadamec & Billen 2012), which affect the trajectories of buoyant diapirs or downwellings interacting with subduction-driven flow in the wedge (Hall & Kincaid 2001; Behn *et al.* 2007; Zhu *et al.* 2009; Hasenclever *et al.* 2011). In these modelling studies, however, mantle wedge deformation capable of producing trench-parallel fast polarizations is relatively localized near the causative slab dip variation or zone of upwelling/downwelling, and does not explain the wider geographic range of observed trench-parallel shear wave splitting fast polarizations.

In our laboratory experiments, we explore how slab dip variations, slab gaps, subduction rate and slab rollback influence 3-D patterns of mantle wedge flow. Our results show that along-trench dip variations lead to significant 3-D complexity in wedge flow. Both the strength of the 3-D flow and the flux of subslab mantle through the gap into the wedge increase as the slab gap size grows and the shallower slab dip decreases. We also quantify the effects of 3-D mantle flow, including cases with rollback, on both wedge anisotropy and on the trajectories of buoyant diapirs rising off of the subducting slab. While we are unable to reproduce the wide extent of observed trench-parallel shear wave splitting fast polarizations (e.g. Fouch & Fischer 1996; Long & Silver 2008; Abt *et al.* 2009), our results highlight strong 3-D time dependence in mantle flow and anisotropy, indicating that the interpretation of seismic and geochemical observations requires a 3-D geodynamic context.

APPARATUS AND EXPERIMENTAL PROCEDURE

A laboratory apparatus is used to model upper-mantle flow in response to subduction (Figs 1c and d). The working fluid is a concentrated glucose solution contained within a 150 cm × 75 cm × 45 cm plexiglass tank. The volume of fluid (4.5×10^5 cm^3) is maintained at constant temperature, resulting in isothermal density and dynamic viscosity values of 1.42 g cm^{-3} and 150 Pa s at 22 °C, respectively (Kincaid & Griffiths 2003).

Kinematic or dynamic forcing may be used to generate slab movement, and in our experiments, subduction is represented kinematically. We employ kinematic subduction for a number of reasons: (1) precise control of relative percentages of downdip and rollback slab motion, (2) control over slab dip and changes in slab dip along the trench, (3) the ability to repeat experiments while refocusing data collection strategies and (4) characterizing wedge response to a systematic variation in a key parameter, while holding other parameters fixed. The dominant mode of mantle flow in subduction zones is driven by the superadiabatic temperature gradient, bound up in the viscous, tabular subducting slab. Slab motion therefore drives a mode of forced convection in an upper mantle that, to first order, is free of competing superadiabatic gradients capable of driving flows of a similar magnitude.

Downdip slab motion is produced using reinforced rubber belts moving around rollers, similar to the method of Hall & Kincaid (2001). The rollers are located at depths equivalent to the upper–lower mantle transition (D_{670}) and the core–mantle boundary (D_{CMB}; at the base of the tank, Fig. 1d). Dip changes are accommodated
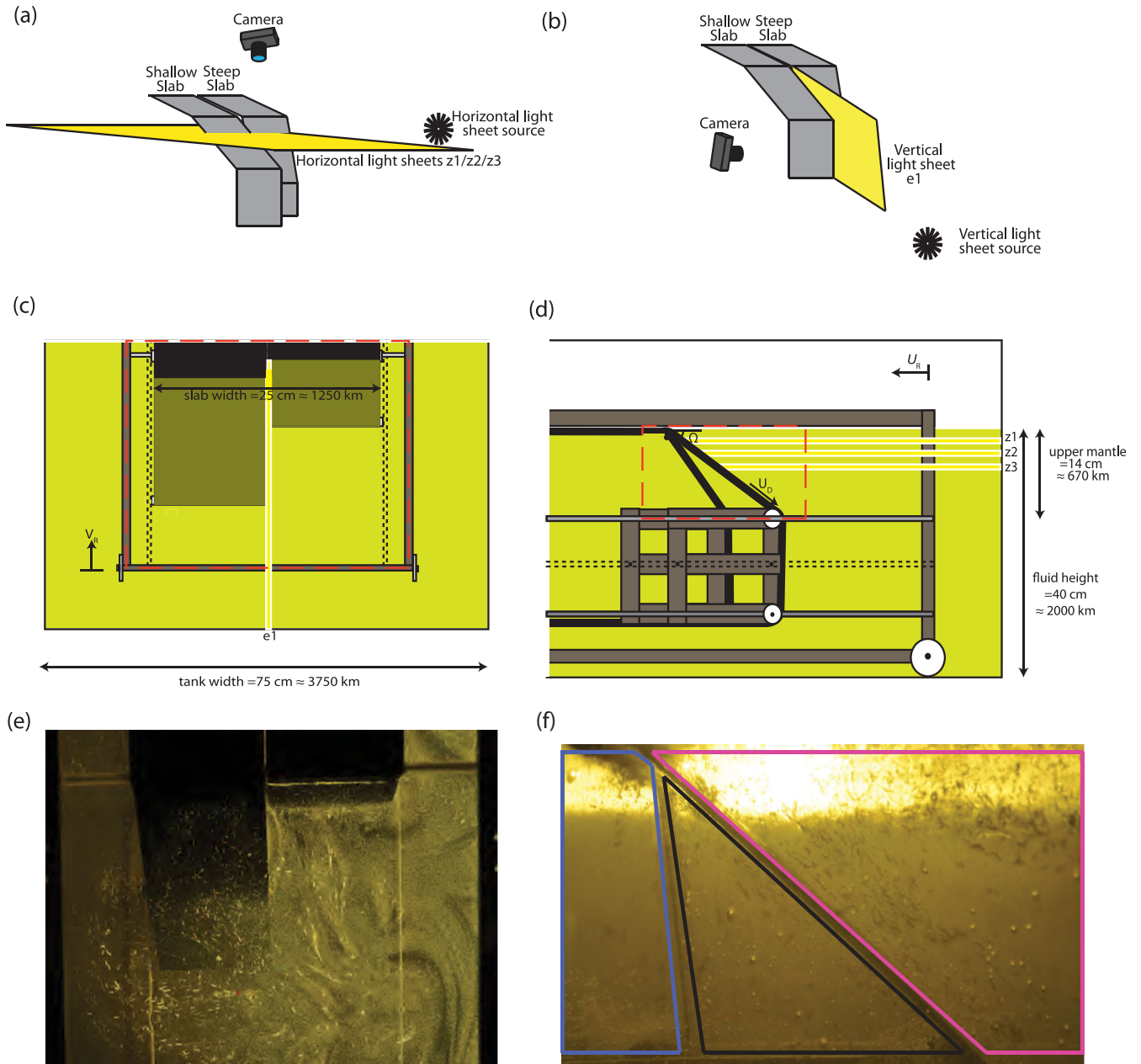
Figure 1. The two different types of light sheet used in our experiments. (a) The horizontal light sheet (z1, z2 or z3), where the entire mantle wedge is illuminated at a constant depth. (b) The vertical light sheet (e1), where a sliver of mantle wedge is illuminated at all depths. (c–d) Diagram of apparatus in map view (c) and cross-section (d). U_D is the downdip subduction rate, U_R is the rollback rate, Ω is the slab dip measured downwards from the horizontal, z1, z2 and z3 are horizontal light sheets and e1 is the vertical light sheet. Red dashed boxes outline the insets shown in (e) and (f). (e–f) Actual images using the corresponding light sheets in (a) and (b) and the area inside the red dashed box in (c) and (d). (f) is a side view of the slabs, with a horizontal light sheet used to illuminate the subslab mantle wedge beneath both slabs (blue shape), the material that is either above the steeply dipping slab or below the shallowly dipping slab (black shape) and the area in the mantle wedge that is above both dipping slabs (magenta shape).

by attaching the rollers to two metal frames that move horizontally; independent translation of the metal frames allows for different dip angles between the two slabs (i.e. belts), creating a slab gap. Rollback motion of the dipping slabs is produced when the large metal frame supporting all belt rollers is drawn backwards at a prescribed, adjustable rate by a low speed, high torque electric motor (e.g. following the method of Buttles & Olson 1998).

Our experiments follow the design of the Kincaid & Griffiths (2003, 2004) kinematic models, except that the fluid in our experiments is isothermal, whereas Kincaid & Griffiths (2003, 2004)

employ surface cooling (i.e. upper thermal boundary layers) to relate subduction style to slab thermal evolution. In these cases, plate rates and modes of downward motion mimic the range of styles observed in time-evolving, 3-D dynamic subduction models (Kincaid & Olson 1987; Griffiths *et al.* 1995; Funiciello *et al.* 2003, 2006; Schellart 2004). The kinematic models are scaled to the mantle using the dimensionless ratio of advection to diffusion, written as the Péclet number

$$Pe = \frac{U_D D}{\kappa}, \tag{1}$$

where U_D is the downdip subduction velocity, D is the upper-mantle depth scale and κ is thermal diffusivity. Time and velocity scales are determined by relating mantle and lab depth scales, including the deepest extent of the dipping part of the slabs at 670 km ($D_{670} = 670$ km $\approx D_L = 14$ cm), and known values for thermal diffusivity ($\kappa_{mantle} = 10^{-2}$ cm^2 s^{-1}; $\kappa_{lab} = 10^{-3}$ cm^2 s^{-1}; Kincaid & Griffiths 2004). 1 min of lab time is equivalent to 5 my of geological time, and a lab plate rate of 1 cm min^{-1} equals a real subducting plate rate of 1 cm yr^{-1}.

While we match the length scales and plate rates of Kincaid & Griffiths (2003), because of the added complexity of variable slab morphology, we choose to begin more simply with the assumption of an isothermal fluid. Motion of the belt generates a velocity boundary layer. However, without thermal gradients, these models do not include the chilled margin of the slab or a cold viscous blanket that characteristically thickens with depth. The lack of thermal gradients, while resulting in a smaller slab thickness, is not expected to significantly alter far-field patterns, because they scale with the half width of the plate, measured in the trench-parallel direction (Buttles & Olson 1998; Kincaid & Griffiths 2003). A more immediate effect is that, with trench-parallel dip variations, the lack of a thermal boundary layer produces a larger slab gap size than would be present with greater slab thicknesses.

Downdip plate velocity is modelled with independent control of speed (U_D) and dip angle (Ω) for two separate belt systems. The speed is controlled by high torque, low-speed motors driving the belts around a series of rollers at either 4 or 8 cm min^{-1} (4 or 8 cm yr^{-1}). In rollback cases, a translation rate of 3 cm min^{-1} (3 cm yr^{-1}) is held constant over a total horizontal distance of 25 cm (1250 km). The total trench-parallel width (W) of the plate is 25 cm (1250 km) (Fig. 1c). Experimental slab dip values range from 30° to 80°, and slab gap sizes, measured as differential dip angle between belts ($\Delta\Omega$), vary from 20° to 50°.

The slab edges are 25 cm (1250 km) from the tank sidewalls, or roughly twice the length scale of the toroidal flow (Kincaid *et al.* 2013). As defined in Funiciello *et al.* (2003), the ratio between the tank width and the slab width is large enough for the flow to be 'volumetrically unconstrained'; the distance between the sidewalls of the tank and the belts is great enough that flow fields, both around the sides of the plate and in the mantle wedge, are not distorted by edge effects due to interaction of the glucose syrup with the walls of the tank (Funiciello *et al.* 2006; Schellart *et al.* 2007, 2011).

Passive Lagrangian markers (whiskers, beads and microbubbles) distributed throughout and moving within the fluid are tracked to provide velocity information in both time and space. Small diameter ($\sim$3 mm), nearly passive Delrin beads (rise rates of the beads through the fluid are $\sim$1 per cent of U_D) are used to track flow rates and patterns within the wedge and to visualize subslab flow through the gap and into the mantle wedge. Whiskers measuring roughly 5 mm in length and 0.1 mm in diameter provide information on velocity and potential olivine lattice preferred orientation (LPO) within the wedge. Large aspect ratio cylinders (whiskers) rotating in viscous shear flows have been shown to follow orientation distribution functions with integrated strain (Jeffery 1922; Buttles & Olson 1998) that closely match theoretical orientation distribution functions derived for the *a*-axis of olivine (Ribe 1989b). Whiskers cannot reproduce the potentially reorienting effects of dynamic recrystallization, but do provide a proxy for the amount and direction of olivine *a*-axis alignment in the absence of dynamic recrystallization. Microbubbles ($\sim$1 mm in diameter) introduced into the fluid during whisker emplacement act as velocity markers, and are

completely passive (i.e. do not rise buoyantly) on the timescales of these experiments.

Wedge flow and whisker alignments are tracked within three 1-cm thick horizontal light sheets centred at depths below the fluid surface corresponding to: z1 = 2 cm (100 km), z2 = 4 cm (200 km), z3 = 7 cm (350 km) (Fig. 1). A single vertical light sheet (e1) oriented along the slab centreline (the trench-normal line that intersects the trench at the gap between the two belts) provides information on vertical velocity (Fig. 1b). Light sheets are produced by light from a slide projector shining through thin horizontal or vertical slits. Covers on the slits are sequentially opened and closed to illuminate individual light sheets. Images are captured at 5-s intervals using high-resolution cameras oriented normal to each light sheet (Figs 1a and b). Continuous cycling allows data to be collected on each sheet at 20-s intervals. Velocities for individual markers are calculated by dividing digitized distance changes between images by the known time interval. Flow patterns are represented as material path lines, or the tracks of parcels of wedge fluid. In time-evolving flows, path lines are distinct from streamlines, the latter of which represent flow at a specific instant in time. The majority of cases employ a stationary trench; however, in an experiment where we add slab rollback (e.g. Exp. 16, Table 1) the top-view camera is coupled to the frame, which translates at the rollback rate. For comparison to the experiments with a stationary trench, position data from the rollback experiment are converted into position data in a fixed reference frame by adding distance for a constant rollback rate of 3 cm min^{-1}.

EXPERIMENTAL RESULTS

In a set of 17 experiments (Table 1), we explore the relationship between complex slab morphology and mantle wedge flow patterns. We begin by describing wedge flow for reference cases where both belts have the same dip, progress to cases where slab dip varies between belts and finally include the effects of trench rollback. Whisker orientations are described at the end of this section.

To describe the experiments, flow patterns are summarized by dividing the wedge into source zones that define the starting points of groups of markers (i.e. whiskers, bubbles or beads) with similar path lines. In addition, we categorize the normalized trench-normal distance (x) as the forearc ($x = 0$–0.25), arc ($x = 0.25$–0.5) and backarc ($x > 0.5$). Velocities are described by the dimensionless marker speed $u^* = \mathbf{u}(x,t)/U_D$, the measured velocity along the path line [$\mathbf{u}(x,t)$] normalized by the subduction rate (U_D); $u_\perp{}^*$ and $u_{||}{}^*$ are the trench-normal and trench-parallel components of the marker speed, respectively. The approach angle (A_w) is the angle of the path line relative to trench-normal (trench-normal = 0° and 180°, trench-parallel = ±90°); the normalized approach angle A_{norm} is equal to A_w divided by 180°. These parameters were measured over a range of normalized distances from the trench, where s_{norm} is the (trench-normal) distance from the trench divided by the total slab width of 25 cm. Plots of $u_\perp{}^*$, $u_{||}{}^*$ and A_{norm} with distance from the trench for select experiments are shown in Appendix A.1. The slab gap, when present, is located along the centreline, and in the figures, the steeper slab is always on the right, and the shallow slab is always on the left.

Wedge flow: downdip reference cases

Results are first presented for reference cases simulating subduction of a single, constant-dip plate segment, without rollback. For

Table 1. The subduction parameters and analysis results for each experiment. Ω_N is the dip of the belt on the right side in Fig. 1(c), Ω_S is the dip of the belt on the left, U_D is the downdip subduction velocity, U_R is the rollback rate, $\mathbf{u}(x,t)$ Max is the maximum horizontal velocity, u^* is the maximum unitless marker speed [maximum marker velocity $\mathbf{u}(x,t)$ Max normalized by U_D], $u_{\parallel}^*$ Max is the maximum trench-parallel component of marker speed (u^*) in each experiment in the area covering the middle of the left-hand belt to the middle of the right-hand belt (=12.5 cm = total belt width/2), and extending 6.25 cm (=total belt width/4) away from the trench and into the mantle wedge. The only exception for this boundary box is for Exp. 16, where, due to the rollback, we extend the box to be 12.5 cm away from the trench and into the mantle wedge. The asterisks next to the $\mathbf{u}(x,t)$ Max value, u^* Max and $u_{\parallel}^*$ Max values for Exp. 4 represent the fact that faster velocities were observed in this experiment than the value shown, but those higher values were from markers experiencing pure toroidal flow (e.g. Fig. 2d, Zone 4), rather than approaching the trench from the mantle wedge, which is our primary area of interest. β is the estimated volume flux through the gap into the mantle wedge. Dashes in the volume flux column indicate that gap flow measurements were not made.

Exp.	Ω_N (°)	Ω_S (°)	U_D (cm min^{-1})	U_R (cm min^{-1})	$u(x,t)$ Max (cm min^{-1})	u^* Max (unitless)	$u_{\parallel}^*$ Max (unitless)	β (cm^3 min^{-1})
1	50	50	8	0	3.6128	0.4516	0.1772	–
2	50	50	4	0	1.7648	0.4412	0.1241	–
3	70	70	8	0	4.1242	0.5155	0.0978	–
4	30	30	8	0	3.1181*	0.3898*	0.0879*	–
5	50	30	8	0	4.0568	0.5071	0.2710	–
6	65	30	8	0	4.4444	0.5555	0.3036	–
7	80	30	8	0	4.9093	0.6137	0.3604	0.7–8.1
8	65	45	8	0	4.8905	0.6113	0.2048	5.3–9.4
9	65	45	4	0	2.1237	0.5309	0.2168	–
10	80	60	8	0	4.9021	0.6128	0.1657	–
11	80	60	4	0	2.5153	0.6288	0.1282	–
12	80	30	4	0	3.1848	0.7962	0.4388	0.7–4.9
14	50	30	4	0	2.279	0.5698	0.3193	–
15	65	30	4	0	2.5592	0.6398	0.3566	0.7–2.6
16, 20	80	30	8	3	8.6228	1.0779	0.3574	4.9–12.0
17	80	30	8	0	5.6264	0.7033	0.3426	–

example, we consider an experiment with an intermediate slab dip (50°) at two different depths (Figs 2a and b, Exp. 1). In the shallowest (z1) light sheet, equivalent to a depth of 100 km from the top of the mantle wedge, subduction drives flow towards the trench through the central portion of the wedge (Zones 2 and 3; Fig. 2a) along path lines that are mostly trench-normal ($A_w \sim 0$ to $\pm10°$) before markers are entrained with the subducting slab. This flow pattern is similar to those of 2-D corner flow models. Wedge circulation differs near the slab edges (Zones 1 and 4), where fluid moves along trench-parallel approach angles ($A_w \sim \pm80°$–90°) before turning downwards with entrained flow above the slab. Some of the fluid is supplied from behind the plane of the slab surface ($A_w > 90°$), as shown in Fig. 2(a). These patterns are replicated at depth (for example at z3, an equivalent depth of 350 km, in Fig. 2b), but with reduced marker speeds. Maximum marker speeds at z1 are nearly three times those at z3, with values of $u^* = 0.35$–0.42 and $u^* = 0.15$, respectively. Because of the dipping slab, path lines in z3 turn downwards with entrained flow at larger values of x, causing some deeper path lines to be orthogonal to those at shallower depths. These vertical gradients in flow direction and speed can create zones of high shear.

Wedge flow varies with slab dip (Figs 2c and d). For example, a steeper slab dip (70°, Exp. 3) produces flow that is more 2-D (Fig. 2c) than the path lines for a dip of 50° (Exp. 1, Fig. 2a). For a dip of 70°, material is drawn towards the slab along primarily trench-normal flow lines originating from Zones 2 and 3, although near the slab edges (Zones 1 and 4), marker trajectories are oblique to the trench (Figs 2c and A1a and f). Shallower dips (30°, Exp. 4, Supporting Information Video S1) result in strongly 3-D flow (Figs 2d and A1b). In contrast to Exp. 3, the fastest flow in this experiment enters the wedge along a trench-parallel trajectory near the slab edges (Figs 2d and A1b, c, e and f), such that both the forearc and arc are supplied along path lines emanating from outside the wedge (beyond the edge of the plate or $|y| > 0.5$). Trench-normal flow near the slab centreline (Zones 2 and 3) is slower and supplies material only to the central third of the slab surface (Figs 2d and A1b, c and d). Maximum

marker speed (u^*) in the z1 layer increases systematically with slab dip; $u^* = 0.39$, 0.45 and 0.52 for slab dips of 30°, 50° and 70°, respectively (Fig. A4).

Wedge flow: trench-parallel slab dip variations

A subset of 12 experiments is used to characterize how trench-parallel changes in slab dip influence wedge flow and the flux of subslab material through a slab gap and into the wedge.

Introducing a difference in the dip of the two slab segments produces asymmetry in wedge circulation in which mantle flow towards the trench is deflected towards the slab segment with the smaller dip. This asymmetry occurs even when the change in dip is relatively small ($\Delta\Omega = 20°$, Exp. 8, Table 1; Fig. 3). While most of the material originating in Zone 3 is entrained downwards above the steeper slab, some wedge fluid closest to the centreline crosses the centreline and is entrained downwards above the shallowly dipping slab. Flow asymmetry also occurs at greater (z3) (Fig. 3b) depths. As in the constant-dip cases, deeper marker speeds are lower, and some z3 path lines are roughly orthogonal to the overlying path lines in z1, indicating significant vertical shear.

Path line patterns, including flow asymmetry created by trench-parallel dip variations, show little change as a function of downdip subduction rate (4 cm min^{-1} versus 8 cm min^{-1}).

Larger trench-parallel dip variations generate stronger flow asymmetry with greater trench-parallel speeds. For example, at z1 in Exp. 10 (slab dips of 80°/60°; Fig. 4a), only mild flow asymmetry is observed, but in Exp. 7 (slab dips of 80°/30°; Fig. 4b, Video S2, Table 1), path lines are strongly deflected in the trench-parallel direction towards the slab segment with the shallower dip, and significant amounts of Zone 3 wedge material are drawn across the slab centreline before downward entrainment. This deflection is reflected by the larger $u_{\parallel}^*$ values (Fig. A2e) and Zone 3 A_{norm} values for $s_{norm} < 0.7$ (Fig. A2f) in Exp. 7 relative to Exp. 10.
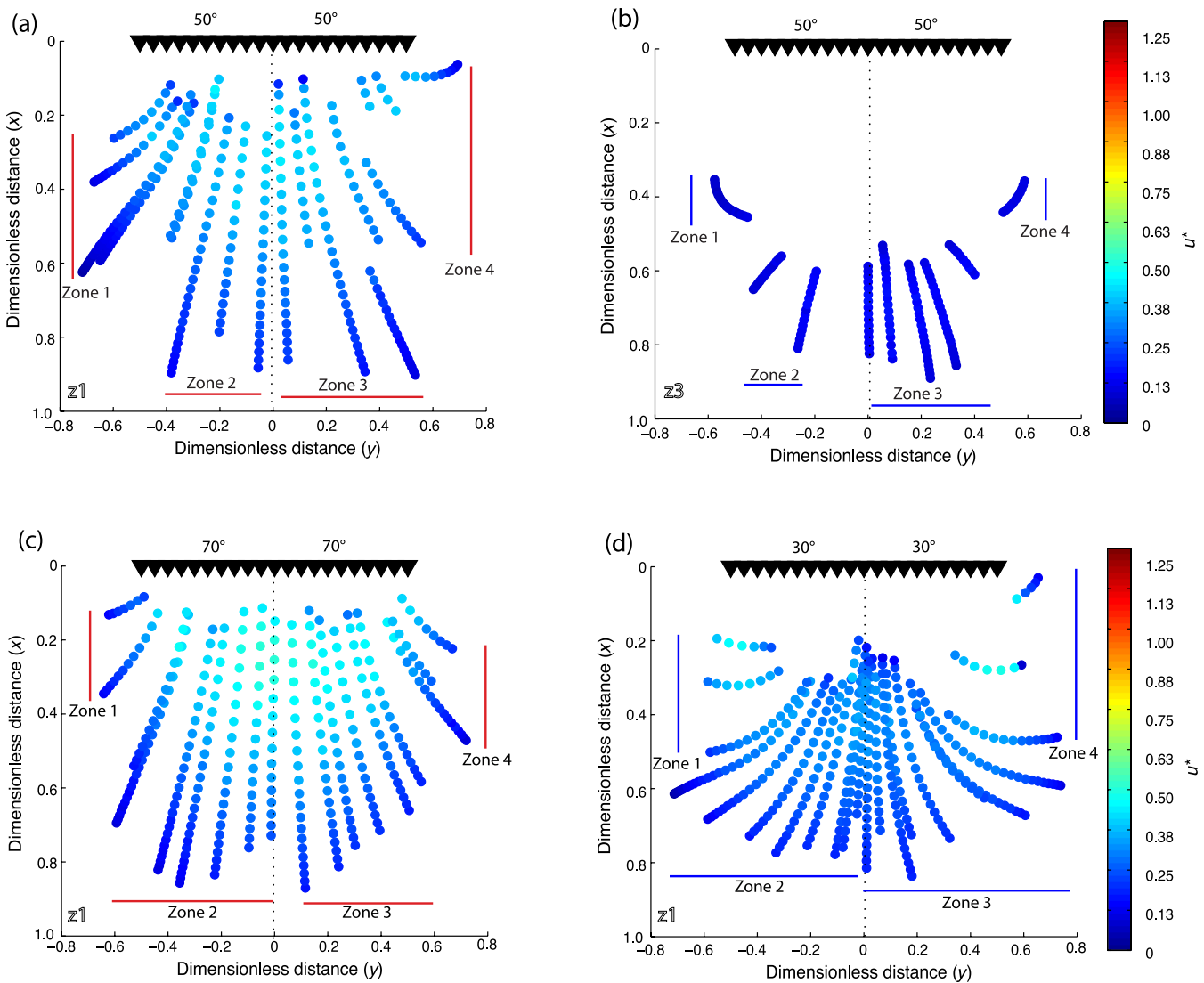
Figure 2. Comparison of Exp. 1 ($U_D = 8\,\text{cm min}^{-1}$, dip = 50°) at depths z1 and z3, and Exps 3 ($U_D = 8\,\text{cm min}^{-1}$, dip = 70°) and 4 ($U_D = 8\,\text{cm min}^{-1}$, dip = 30°) at depth z1. Map view plots at depths (a, c–d) z1 (=2 cm ≈ 100 km) and (b) z3 (=7 cm ≈ 350 km) are shown. Individual circles represent motion of a single marker through time. Colours represent dimensionless flow rate (=u^*). Black lines with triangles show the location of the trench. Slab segment dip values are displayed above their corresponding halves of the trench. The dotted line represents the slab centreline. Locations are given as distance in trench-parallel (y) and trench-normal (x) directions, normalized by total plate width ($W = 25\,\text{cm}$) relative to an origin along the slab centreline at the trench. (a) Markers moving within the shallow wedge at z1 (depth of 2 cm ≈ 100 km) show four distinct zones of flow and resupply to the slab surface (red lines): 1. Material originating in the mantle wedge at the outer edge of the left-hand slab. 2. Material originating in the mantle wedge between $-0.4 < y < 0$. 3. Material originating in the mantle wedge between $0 > y > 0.55$. 4. Material originating in the mantle wedge above the outer edge of the right-hand slab. (b) Similar plot to (a), but at z3 (depth of 7 cm ≈ 350 km). (c) Path line plot of Exp. 3 at depth z1. (d) Path line plot of Exp. 4 at depth z1.

The wedge flow asymmetry created by trench-parallel slab dip changes is consistent with 2-D analytical pressure solutions (Fig. A5; Appendix A.2) and numerical results (Hall *et al.* 2000; Kneller & van Keken 2007; Kneller & van Keken 2008). Non-hydrostatic pressures from 2-D corner flow in the mantle wedge are more negative (Fig. A5, top row) and trench-parallel pressure gradients are higher above the shallowly dipping slab (Fig. A5, middle row). In cases where a slab gap is present, markers in Zones 3 and 4 are responding to three different drivers: the trench-parallel pressure gradient, which is strongest in the forearc and pulls wedge material from the steeply dipping slab to the shallowly dipping slab (Fig. A5), the subduction velocity boundary condition imposed by encountering the part of the shallow belt close to the slab

centreline and the normal entrainment flow of the steeply dipping slab.

Maintaining a similar slab dip variation, but steepening both plate dips leads to weaker trench-parallel flow close to the slab and the slab centreline (Fig. 5). This trend is evident when comparing Exp. 10 (dips of 80°/60°; Fig. 4a), Exp. 8 (dips of 65°/45°; Fig. 3a) and Exp. 5 (dips of 50°/30°), which have maximum $u_\parallel^*$ values of 0.17, 0.21 and 0.27, respectively (Figs 5a and b, Table 1). The experiments with the same dips but a downdip velocity of 4 cm min^{-1} (Exps 11, 9 and 14) produce a similar $u_\parallel^*$ trend (0.12, 0.22 and 0.32, respectively). However, steepening both dips does not yield clear trends in total maximum marker speed (u^*) (Figs A4a and b, Table 1), as seen in Exps 10, 8 and 5 ($U_D = 8\,\text{cm min}^{-1}$), where u^* values are 0.61, 0.61
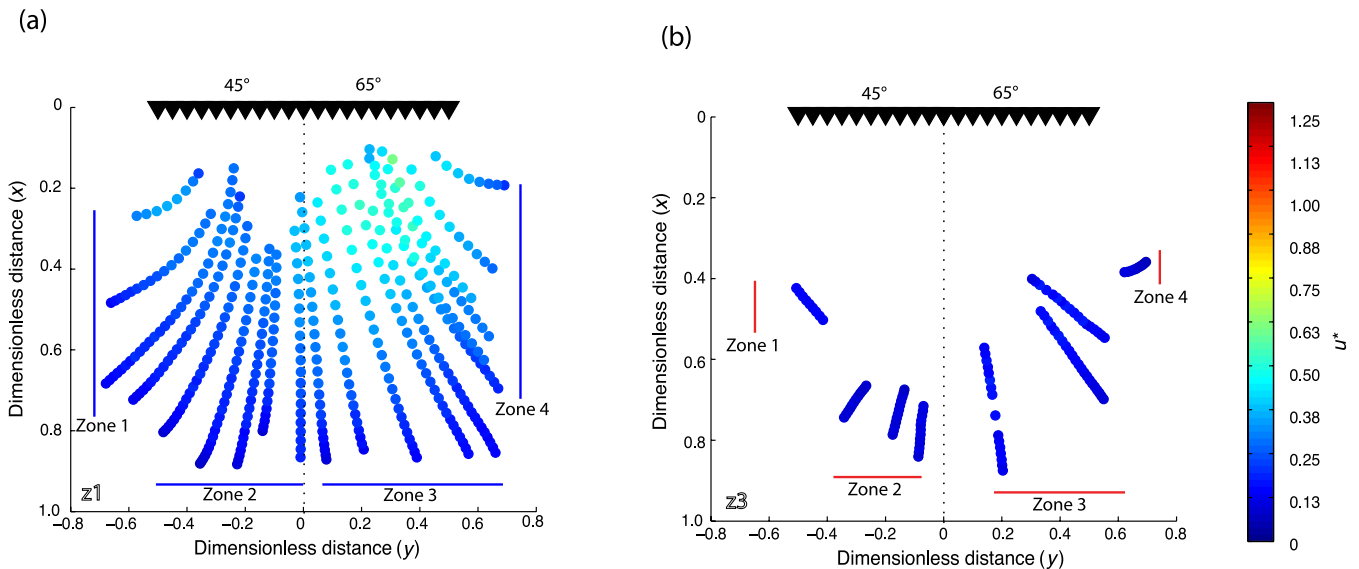
(a)

(b)

Figure 3. Comparison of Exp. 8 ($U_D = 8$ cm min^{-1}) at depths z1 and z3. Exp. 8 has a steep dip of 65°, a shallow dip of 45° and is plotted at depths (a) z1 ($=2$ cm ≈ 100 km) and (b) z3 ($=7$ cm ≈ 350 km). Individual circles represent motion of a single marker through time. Colours represent dimensionless marker speed. Black lines with triangles show the location of the trench. The black dotted line represents the slab centreline. Slab segment dip values are shown above their corresponding halves of the trench. Locations are given as distance in trench-parallel (y) and trench-normal (x) directions, normalized by total plate width ($W = 25$ cm) relative to an origin along the slab centreline at the slab surface. The discontinuous path line in Zone 3 of (b) represents a whisker that was just on the boundary of the z3 light sheet; it would sometimes sink below and then reenter the z3 layer.
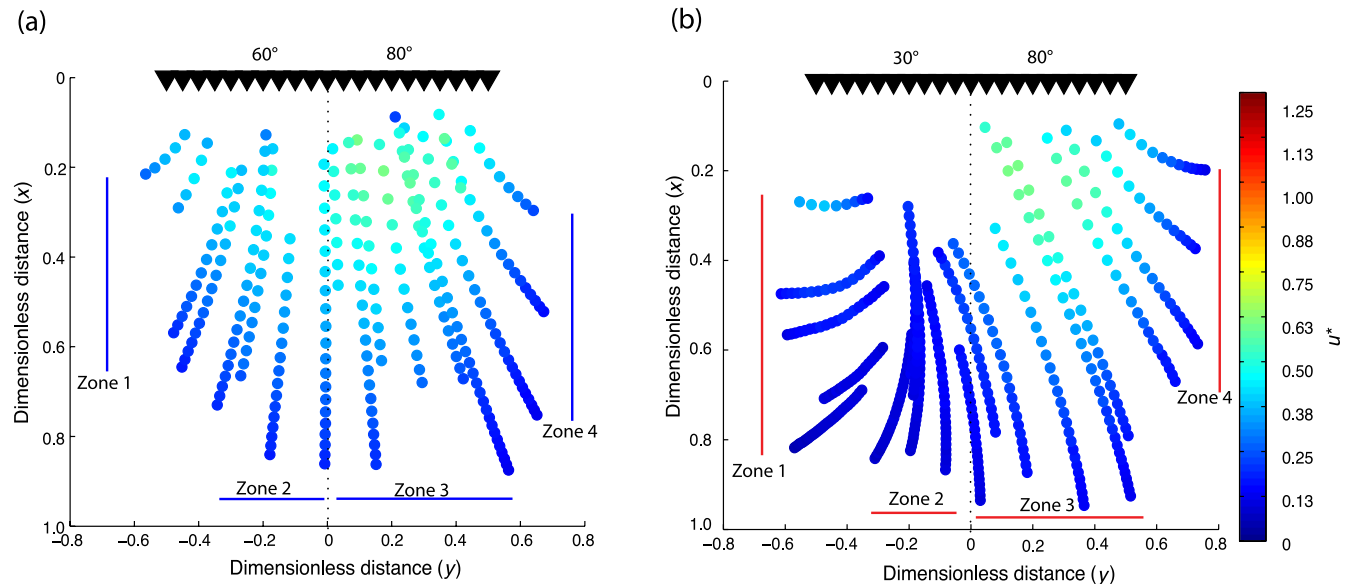
(a)

(b)

Figure 4. Comparison of Exps 10 ($U_D = 8$ cm min^{-1}) and 7 ($U_D = 8$ cm min^{-1}) at depth z1. Path line plots for (a) smallest gap size at the steepest possible dips (60°/80°, Exp. 10) and (b) the largest gap size (30°/80°, Exp. 7) are shown. Black lines with triangles show the location of the trench. The black dotted line represents the slab centreline. Slab segment dip values are displayed above their corresponding halves of the trench.

and 0.51, and for Exps 11, 9 and 14 ($U_D = 4$ cm min^{-1}), where u^* values are 0.63, 0.53 and 0.57.

Wedge flow: slab rollback

Trench/slab rollback significantly modifies the 3-D asymmetric flows generated by the presence of trench-parallel dip variations. In Exp. 16 (Video S3, Table 1, Fig. 6), 3 cm min^{-1} of rollback is added to the case with dips of 80°/30° and a U_D of 8 cm min^{-1} (Exp. 7, Table 1). With slab rollback, shallow (z1) path lines

(Fig. 6a) are still highly asymmetric, with path lines from Zones 3 and 4 crossing the slab centreline before turning downwards with entrainment above the more shallowly dipping slab. The curvature of path lines in Zone 3 moving towards the shallow slab in Exp. 16 (clockwise in map view) has the opposite sense from Zone 3 transport paths in the similar, but non-rollback case of Exp. 7 (counter-clockwise in Fig. 4b). This difference in curvature is reflected in normalized approach angle values for Zone 3 in both experiments (Fig. A3f). Both trench-parallel (Fig. A3e) and trench-normal (Fig. A3d) flow rates are significantly higher in the case with rollback.
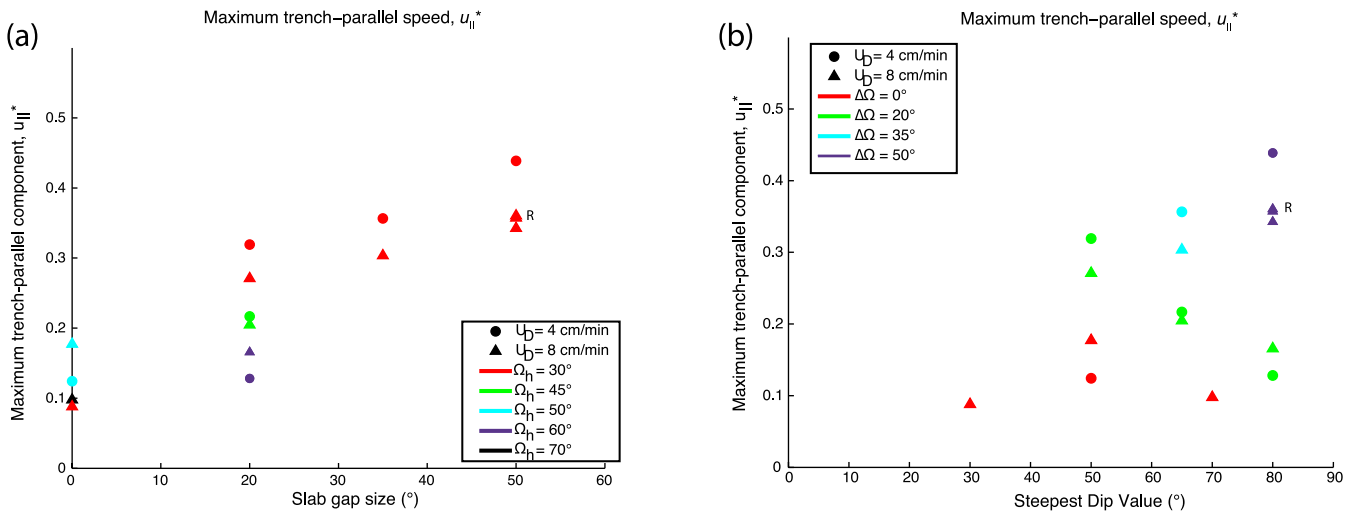
(a)

(b)

Figure 5. Summary of maximum trench-parallel speeds ($u_{||}^*$), plotted according to both slab gap size ($\Delta\Omega$) and steepest dip value. (a) Maximum trench-parallel speed $u_{||}^*$ in each experiment, calculated over each path that had points within a box with width $W/2$ (=12.5 cm) along the trench, centred on the slab centreline and extending $W/4$ (=6.25 cm) from the trench into the mantle wedge. With rollback, we change the box size to extend $W/2$ (=12.5 cm) from the trench into the mantle wedge to account for the greater spatial extent inherent in the rollback case. $\Delta\Omega$ represents the slab gap size, and Ω_h represents the shallowest dipping slab in a given experiment. The 'R' in both (a) and (b) represents the values for Exp. 16, which is the only experiment where we added slab rollback. (b) represents the same data as in parts (a); we have changed the x-axis in this diagram to illustrate that the gap size, rather than the steepest dip value, drives the increase in $u_{||}^*$.
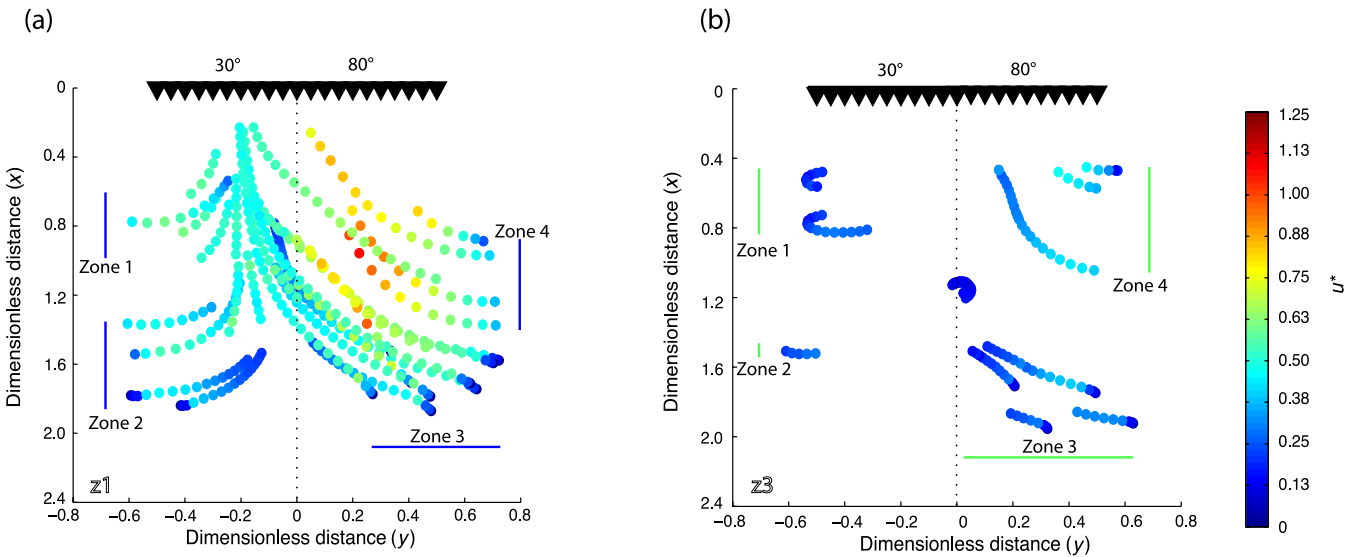
(a)

(b)

Figure 6. Comparison of Exp. 16 ($U_D = 8$ cm min^{-1}, $U_R = 3$ cm min^{-1}) at depths z1 and z3. The plots for an experiment with both the maximum slab gap size and rollback (Exp. 16) at depths of (a) z1 (=2 cm ≈ 100 km) and (b) z3 (=7 cm ≈ 350 km) are shown. Black lines with triangles show the location of the trench. The dotted line represents the slab centreline. Slab segment dip values are shown above their corresponding halves of the trench.

Rollback also drives vigorous toroidal flow around the edges of the slab at greater depths in the wedge (e.g. level z3 in Fig. 6b). Fluid parcels close to the retreating slab in Zone 1 at level z3 first move out from the wedge with strong trench-parallel motion and then back into the wedge after passage of the slab. Once the slab passes, deeper path line trajectories (z3) are more similar to those at z1. As in previous cases, marker speeds at z3 are much lower than those at z1 (e.g. marker 3a in Fig. A3c).

Wedge flow: summary of flow velocities and drivers

In summary, $u_{||}^*$ values systematically vary as a function of trench-parallel dip variation ($\Delta\Omega$ or slab gap size; Table 1 and Fig. 5), but u^* behaviour is more complex. As previously mentioned, with no slab gap ($\Delta\Omega = 0°$), steeper dips drive greater maximum u^* values in the wedge (Fig. A4a). When trench-parallel slab dip variations exist, maximum u^* is strongly correlated with greater $\Delta\Omega$ (Fig. A4b), but does not systematically increase with greater values of the steepest slab dip (e.g. the u^* values for $\Delta\Omega = 20°$ in Fig. A4a). As for maximum $u_{||}^*$ values for the central wedge closest to the trench (defined by $x \leq 0.25$ and $-0.5 \leq y \leq 0.5$), larger trench-parallel slab dip variations generate greater $u_{||}^*$ values and stronger flow asymmetries (Fig. 5a). When a slab gap is present, and for a given value of $\Delta\Omega$, $u_{||}^*$ increases as the dips of both slabs decrease (see the points for $\Delta\Omega = 20°$ in Figs 5a and b). This result is consistent with the increase in trench-parallel pressure gradient predicted for the mantle wedge above more shallowly dipping slabs (Fig. A5). Finally, the addition of slab rollback increases wedge flow velocities,
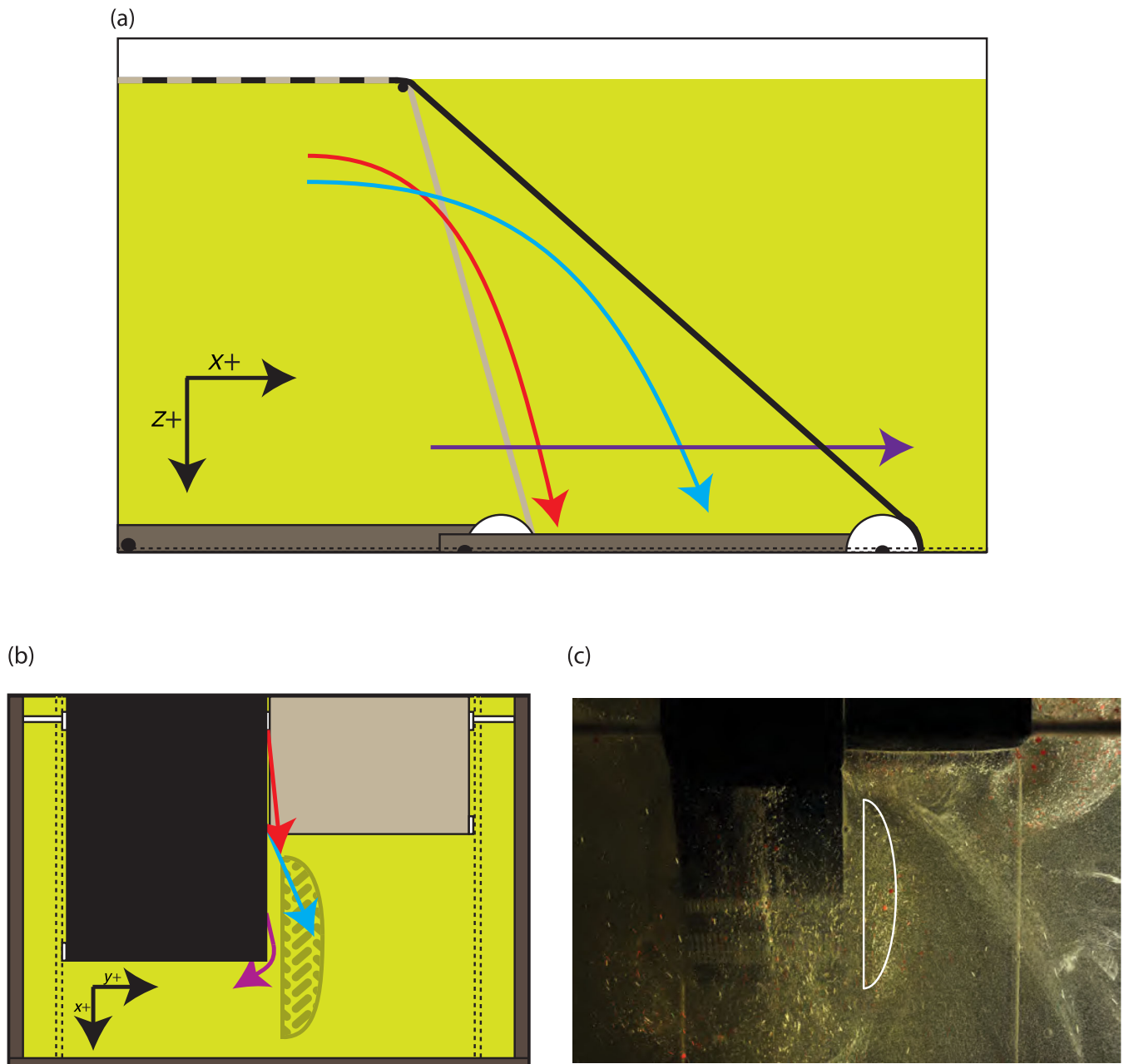
Figure 7. Schematic diagrams of observed paths of subslab mantle flowing through the gap and into the mantle wedge in (a) cross-section and (b) map view. The zone in the mantle wedge where subslab material, following the trajectory through the slab gap indicated by the blue line, can reside before being subducted is denoted by the shaded shape. (c) Photo from an experiment with the maximum slab gap size and subduction rate (Exp. 17), where the shaded zone in (b) is outlined in white.

and the highest measured u^* value in all of our experiments is found in Zone 4 of Exp. 16 ($u^* = 1.08$, labelled 'R' in Figs A4a and b), above the steeply dipping slab. Rollback does not significantly change the maximum $u_{||}^*$ value (Figs. 5a and b), indicating that the increase in marker speed close to the retreating slab ($x \leq 0.5$) partitions primarily into trench-normal velocity.

Flow through slab gaps

We measured flow from beneath the slab, through the gap and into the mantle wedge in order to evaluate the implications of this flow for shear wave splitting patterns and geochemical data in subduction zone mantle wedges near hypothesized slab tears or gaps (e.g.

Russo *et al.* 2010). By seeding the subslab mantle material with bubbles and red beads, we observed subslab flow penetrating the mantle wedge in all cases where $\Delta\Omega \geq 35°$, and in only one case where $\Delta\Omega = 20°$ (Table 1). We observed three different trajectories of subslab material penetrating the mantle wedge (Fig. 7). A number of tracers emerge from beneath the shallow slab and enter the mantle wedge above the shallowly dipping slab (purple path in Fig. 7). Other markers escape into the mantle wedge above the steeply dipping slab (blue path in Fig. 7; also Fig. A6a), while others barely enter the mantle wedge before being entrained either above or along the edge of the steeper slab (red path in Fig. 7). Larger gaps increase the likelihood of subslab flow through the gap, but do not necessarily cause higher gap flow rates. For example, the highest

measured through-gap speed without rollback occurred in Exp. 8, with $\Delta\Omega = 20°$.

Rollback increases rates of mantle flow through the slab gap, as expected when the translating plate displaces subslab fluid. In cases with rollback, marker speeds through the gap range from $u^* = 0.19$–0.46; these values are equivalent to 1.5–3.7 cm min^{-1} = 1.5–3.7 cm yr^{-1} (e.g. Fig. A6b). In cases without rollback, marker speeds through the gap are $u^* = 0.05$–0.36 (equivalent to 0.2–2.9 cm min^{-1} = 0.2–2.9 cm yr^{-1}). Similarly, cases with rollback yield significantly higher volume fluxes (β in Table 1) through the gap (4.9–12.0 cm^3 min^{-1} ≈ 0.12–0.30 km^3 yr^{-1}) than those cases without rollback (0.7–9.4 cm^3 min^{-1} ≈ 0.02–0.24 km^3 yr^{-1}) (method described in Appendix A.3).

Larger gap sizes lead to increased intrusion of subslab tracers into the wedge. The furthest penetration of subslab markers into the mantle wedge prior to downward entrainment (up to 17 cm or ∼850 km away from the trench) occurred in a large gap case (Exp. 17) where a bead entered the wedge above the more steeply dipping plate. We do not observe an upward component of motion for markers traversing the gap, suggesting that other conditions (e.g. possibly the onset of backarc spreading) are required for gap material to be sampled by decompression melting processes. Contrary to the geochemical observations of Klein & Karsten (1995) and Karsten *et al.* (1996), we find no evidence for penetration of mantle wedge material into the subslab mantle.

Whisker orientations

The evolution of whisker azimuths from an initially random distribution provides information on potential seismic anisotropy. As discussed previously, whiskers are good first-order approximations for LPO formation from olivine *a*-axis alignments, but do not include the effects of dynamic recrystallization.

With a constant slab dip (Exp. 4, Fig. 8a), whiskers generally rotate to orientations that are parallel to subparallel to their path lines. Exceptions to this rule occur close to the slab centreline, where path lines are in general trench-normal and little rotation in the *x*–*y* plane occurs, and on select paths that involve toroidal flow close to the edges of the slab (e.g. Zone 1 nearest to the trench; Fig. 8a). In the case of a large slab gap and no rollback (Exp. 7; Fig. 8b), the zone near the slab centreline is no longer a zone of low whisker rotation, due to the high rates of *x*–*y* plane shear involved in the flow drawn over to the shallowly dip slab as it approaches the trench. With the addition of rollback (Exp. 16; Fig. 8c), the strongest rotation of whisker alignments towards their path lines again occurs in the group of paths that converges above the shallowly dipping slab (Zones 2 and 3).

Trench-oblique and trench-parallel whisker orientations are generally found on two types of path lines: (1) path lines that are the most deflected from trench-normal, across the slab centreline from the steeply dipping slab to the shallowly dipping slab, with rapid rotation along the path, or (2) path lines that bring flow into the wedge from around the edge of the slab. To quantify these patterns, we measured the orientations of every whisker within each horizontal light sheet (z1, z2, z3) in one late-stage [time elapsed ≈ 8 min (≈40 my)] photograph for two similar experiments, where the only difference was the absence (Exp. 17) or presence (Exps 16 and 20, Table 1) of trench rollback. Exps 16 and 20 (Exp. 16/20 hereafter) have identical subduction parameters (Table 1), and we have combined their results to obtain more robust whisker orientation distributions.

Whisker azimuths at all three depths of Exp. 17 (Fig. 9, Column I) and Exp. 16/20 (Fig. 9, Column II) are displayed in rose diagrams placed in their corresponding model blocks. Each block measures 5 cm (250 km) in the trench-parallel direction and 6.25 cm (312.5 km) in the trench-normal direction (Fig. 9). Rose diagrams are only plotted for blocks that contain four or more whiskers, with the exception of model block 10 in Exp. 16/20 at z3. While this block contained only two whiskers, it was retained to enable comparison with Exp. 17 at a full range of depths.

Most mean whisker orientations lie within 45° or less of trench-normal. More trench-parallel mean whisker alignments occur near the slab edges, where toroidal flow is present (e.g. block 20 in z1 of Fig. 9, Column II), or close to the slab gap above the steeply dipping slab where flow is deflected towards the shallowly dipping slab (e.g. block 14 of Exp. 17, Figs 9 and 10). The observed trench-parallel deflection of whisker orientations near the slab centreline occurs on roughly the same length scale [one block with dimensions of 5 cm by 6.25 cm (250 km by 312.5 km)] as that seen in the 'trench-parallel stretching' of Kneller & van Keken (2007, 2008), although our whisker orientations are more trench-oblique than truly trench-parallel. In contrast, the addition of rollback (Exp. 16/20) causes the whiskers near the centreline to have trench-normal alignments, due to the stronger trench-normal flow near the centre of the model produced by toroidal flow (Fig. 9, Column II), in agreement with previous studies (e.g. Funiciello *et al.* 2003, 2006; Kincaid & Griffiths 2003; Druken *et al.* 2011).

To illustrate how whisker orientations at the steep-to-shallow slab transition are affected by rollback, we examined whiskers azimuths in both the backarc (model block 10) and the arc (model block 14) at the slab centreline for cases both with (Exp. 16/20) and without (Exp. 17) rollback (Fig. 10). Model block 14 is close to the area that experiences the highest marker speeds due to the presence of a slab dip variation (e.g. Fig. 4b); it is representative of flow near the slab gap. Model block 10 is representative of flow further from the slab gap. At all three depths in block 14, the whisker azimuth averages in the case without rollback (Exp. 17) are deflected further away from trench-normal and have larger standard deviations, which represent the wider range of observed whisker azimuths (Fig. 10). The effect of rollback on whisker alignment is relatively localized. Whiskers in the backarc (block 10) in both experiments are similar, maintaining an orientation just counter-clockwise of trench-normal orientations at all depths, although the whiskers in the case with rollback (Exp. 16/20) have less scatter (Figs 9 and 10). In addition, block 17 whiskers, further away from the gap, in fact become more trench-parallel with rollback (Fig. 9).

Near the slab gap (block 14) in the case with no rollback, whisker alignments rotate significantly with depth in the counter-clockwise direction towards the shallowly dipping slab (Fig. 10). (The sense of rotation was determined by observing the counter-clockwise rotation of whiskers at the centreline near the slab gap in real time.) In contrast, with rollback (Exp. 16/20), whisker azimuths in block 14 rotate clockwise with depth (Fig. 10). The implications of these results for shear wave splitting in subduction zone mantle wedges are explored in the next section.

IMPLICATIONS

Geochemical anomalies and melt migration

In all of our experiments with trench-parallel slab dip variations, three types of mantle wedge flow are present: strong toroidal flow,
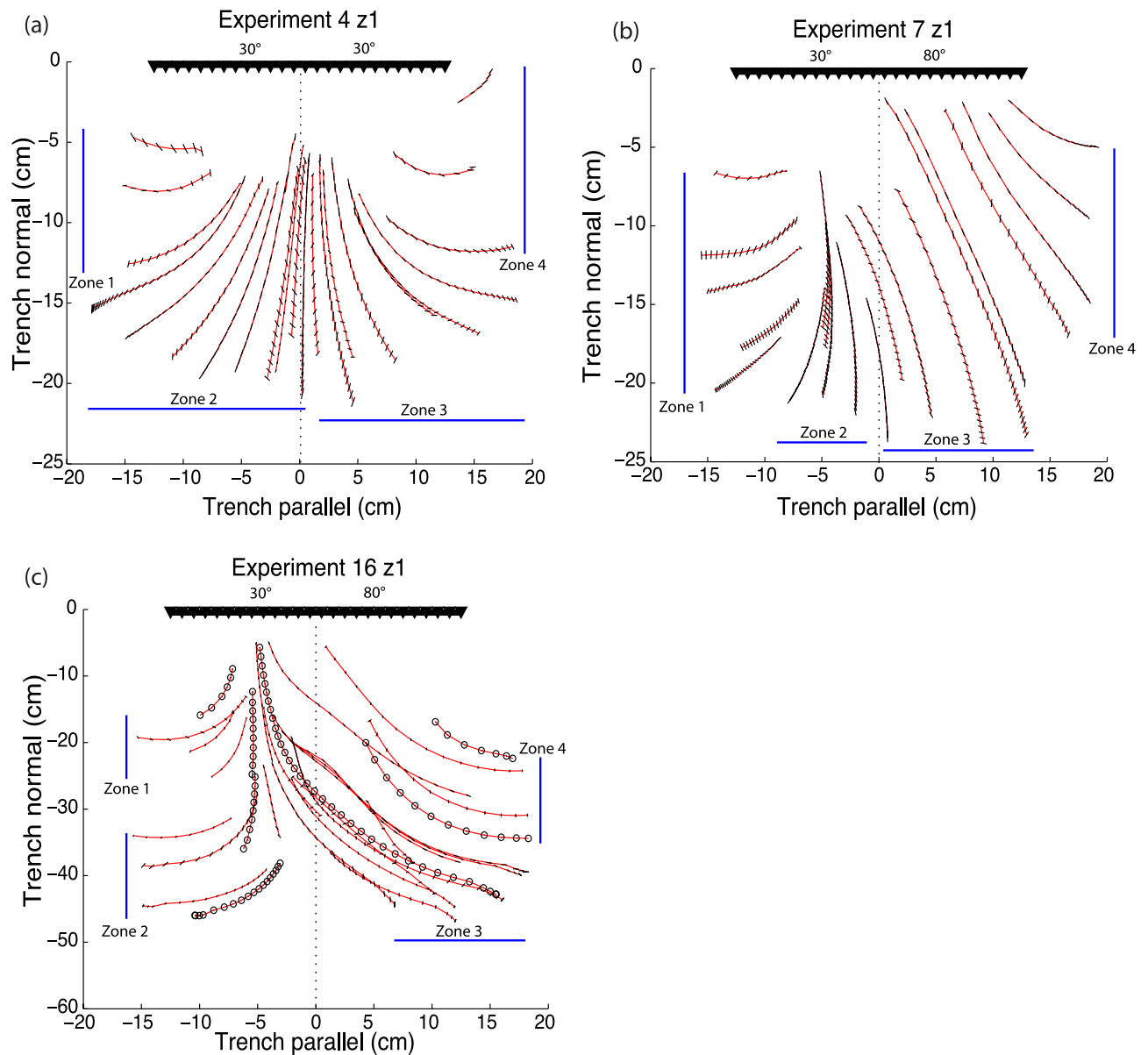
Figure 8. Path lines and whisker orientations for (a) Experiment 4, (b) Experiment 7 and (c) Experiment 16. Red lines represent the path line vector orientation from one time step to the next, and the black lines represent whisker orientations at a time step. The black dotted line represents the slab centreline. Zones from previous figures are denoted by the blue lines. Black circles indicate a bubble or bead, rather than a whisker, and thus provide us with no information about the rotation along a path line. Slab segment dip values are displayed above their corresponding halves of the trench.

trench-oblique flow towards the shallowly dipping slab and slab gap through-flow into the mantle wedge. Geochemical data provide evidence for such flows in real subduction zones. In the Tonga subduction zone, Samoan hotspot magmatic signatures, originating from beneath the subducting Pacific Plate, have been recorded in magmas in the northern Lau Basin, a backarc spreading centre on the overriding Australian Plate (e.g. Turner & Hawkesworth 1998). A trench-parallel component of toroidal flow, propagating around the slab edge and laterally into the wedge, is also supported by evidence of mixing between mantle wedge material and Samoan hotspot material further south along the trench (Falloon *et al.* 2007; Regelous *et al.* 2008). Geochemical evidence for trench-parallel flow in the mantle wedge has also been found in the Calabrian (e.g. Faccenna *et al.* 2005) and central American (e.g. Hoernle *et al.*

2008; Gazel *et al.* 2011) subduction zones. Flow through a slab gap or slab window is also detectable with geochemistry, whether it be the influx of subslab mantle material into the mantle wedge after slab detachment (Ferrari 2004; Macera *et al.* 2008; Guo *et al.* 2011; Pan *et al.* 2012) or the subduction of a spreading centre (D'Orazio *et al.* 2000; Abratis & Worner 2001; Gutiérrez *et al.* 2005; Guivel *et al.* 2006).

We use our experimental results to demonstrate the importance of 3-D flow fields in controlling surface geochemical patterns at subduction zones. We track theoretical diapirs (i.e. material rising vertically off of the slab) moving with imposed buoyant rise rates through our highly heterogeneous wedge flow fields. Exps 3, 8 and 16 (Table 1) are used to develop the diapir trajectory models because they provide sufficient path line data at all three depths. After finding
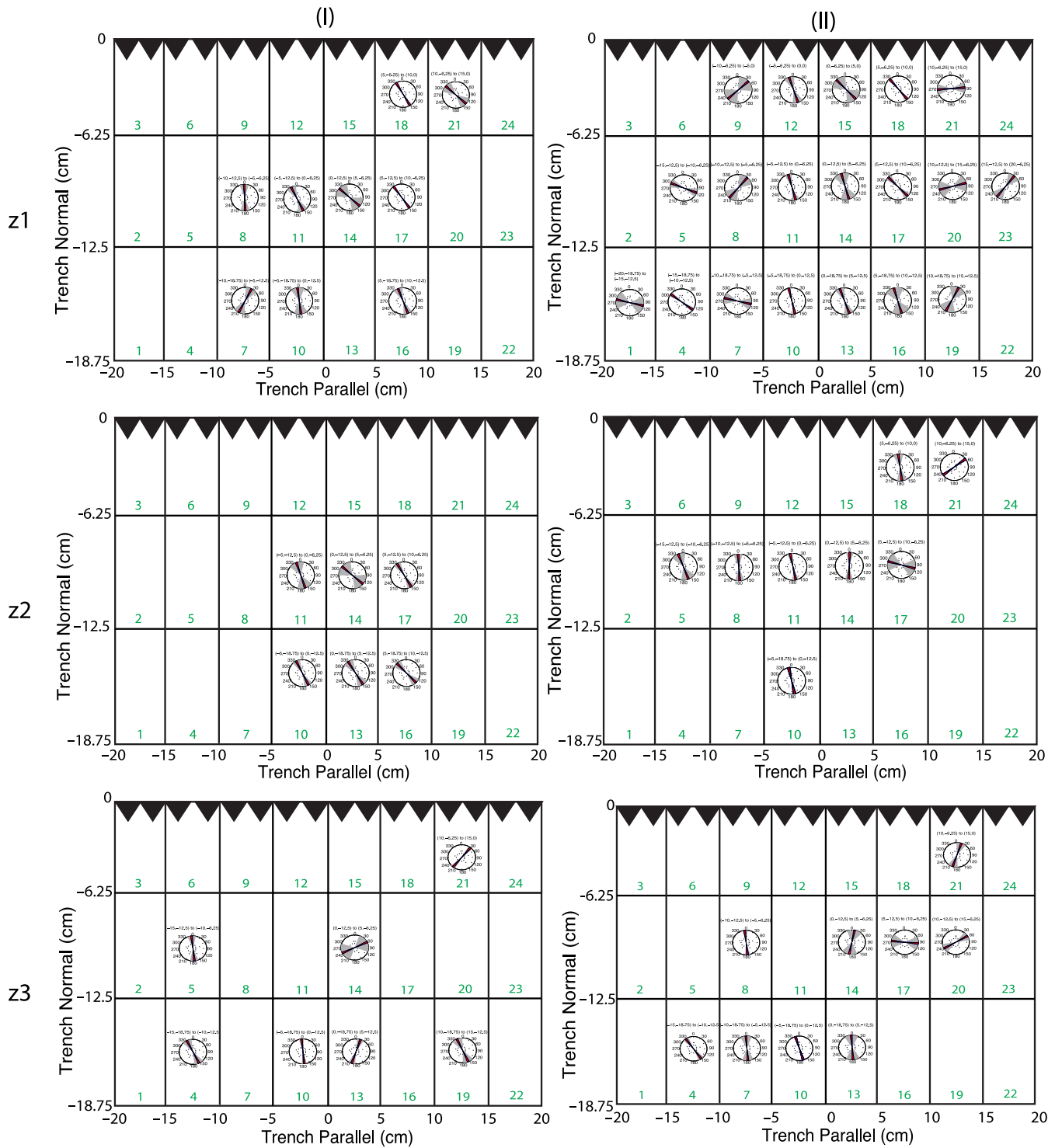
Figure 9. Rose diagrams of whisker orientations within a given model block for (I) an experiment with the maximum slab gap size and maximum downdip subduction rate (Exp. 17) and (II) an experiment with the maximum slab gap size, maximum downdip subduction rate and a rollback rate of 3 cm min^{-1} (Exp. 16/20). The three light sheets are designated by z1, z2 and z3. Red lines indicate the average whisker azimuth for that model block, and the grey zone surrounding the red indicates the standard deviation of the whisker orientations. The numbers in green are the model block numbers referred to in the text.

two places in Exps 3, 8 and 16 where we have (close-to) overlapping path lines at all three depths, we place a theoretical diapir at a depth of 375 km and, for three different rise rates ($V_P = 1.5$, 2.5 or 8 cm yr^{-1}, eq 2),

$$V_P = \frac{B}{n_{\text{rise}}}, \tag{2}$$

we calculate the propagation distance of the diapir along the path line at each depth (3).

$$q_{\text{h}} = q|_{o+n_{\text{rise}}} . \tag{3}$$

B is the known distance from the bottom of one layer to the next, n_{rise} is the number of time steps it takes for the diapir to rise from one
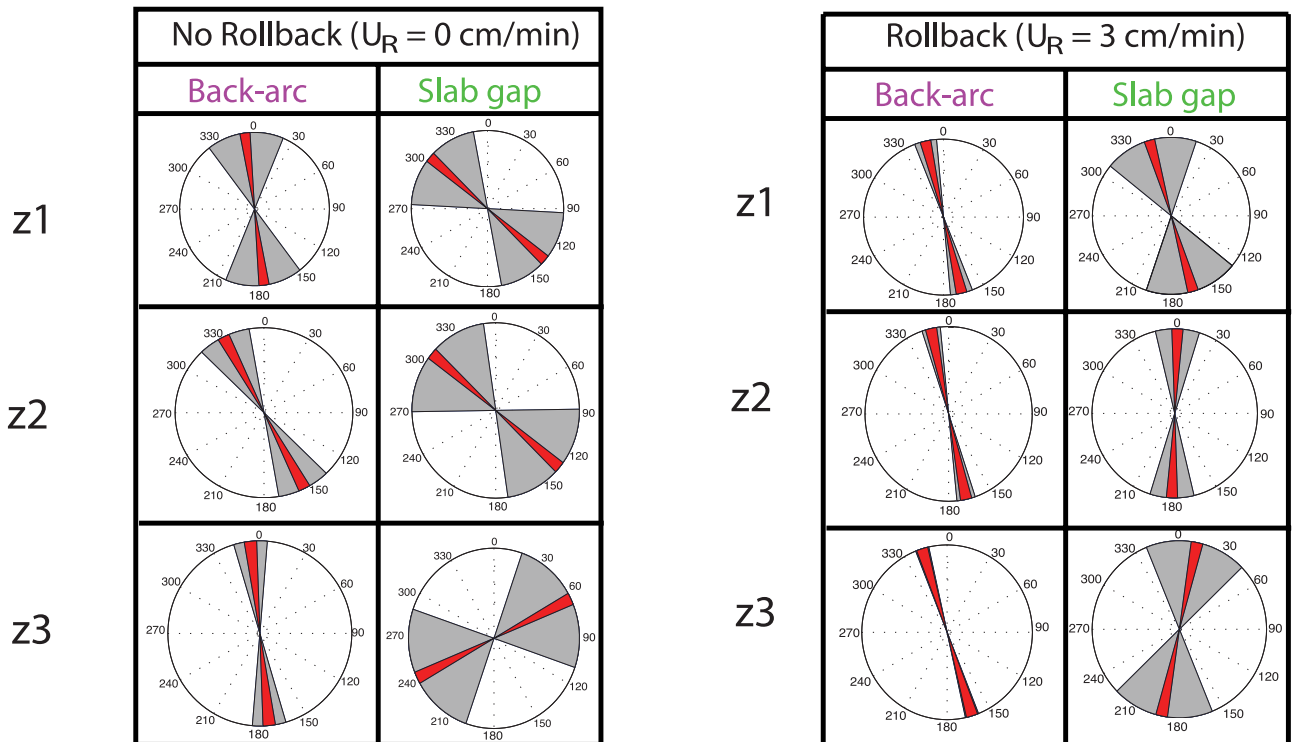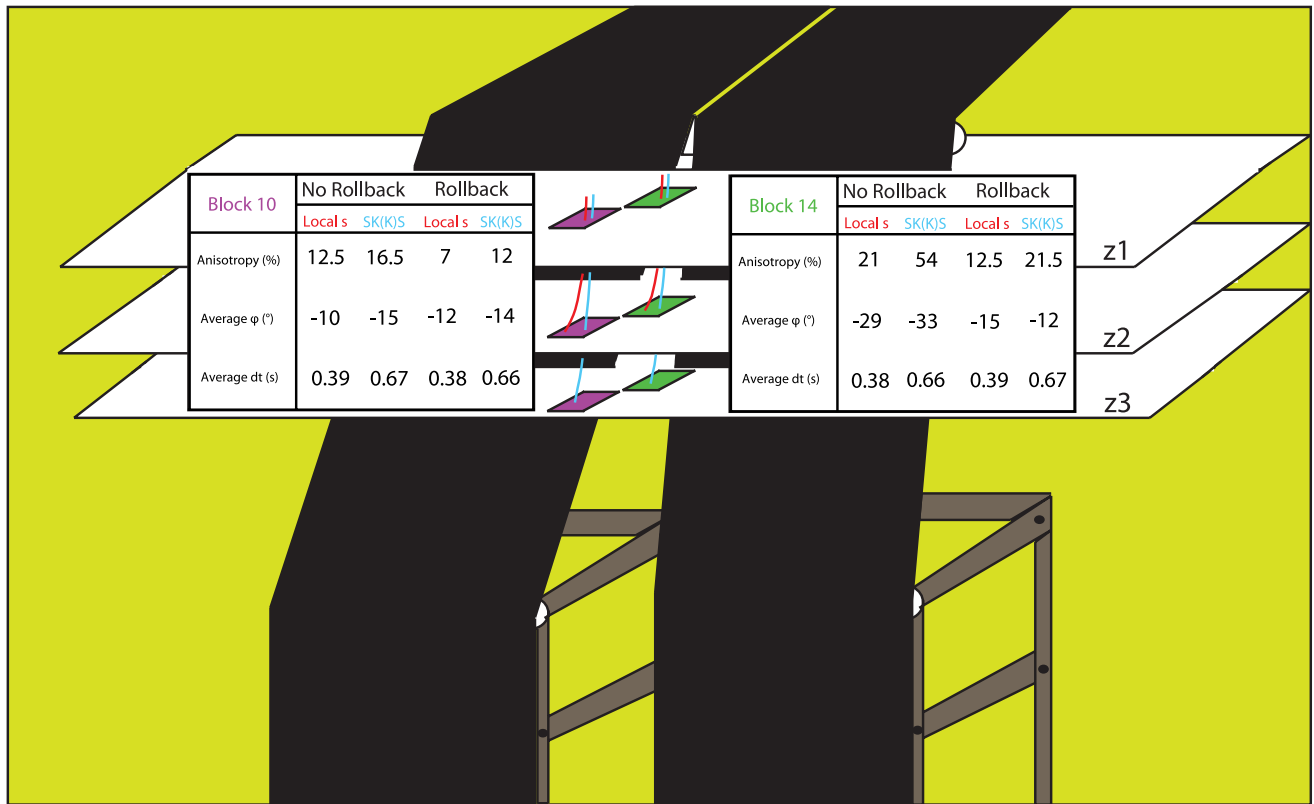
Figure 10. Whisker azimuth rose diagram comparison between two experiments with the same maximum slab gap size and maximum downdip subduction rate; the only difference is the lack [Exp. 17 ('No Rollback')] or presence [Exp. 16/20 ('Rollback')] of rollback. We compare a model block located near the slab gap over the steeply dipping slab (block 14, at the slab gap, green) and a block further in the backarc over the shallowly dipping slab (block 10, in the backarc, purple). Averaged shear wave splitting fast directions (φ) and splitting times (dt) are included for blocks 10 and 14 for local s (red ray paths) and $SK(K)S$ (blue ray paths) phases. Anisotropy percentages are those that generate the average dt values that most closely match the benchmark values discussed in the text. Original synthetic results are displayed in Table S1.
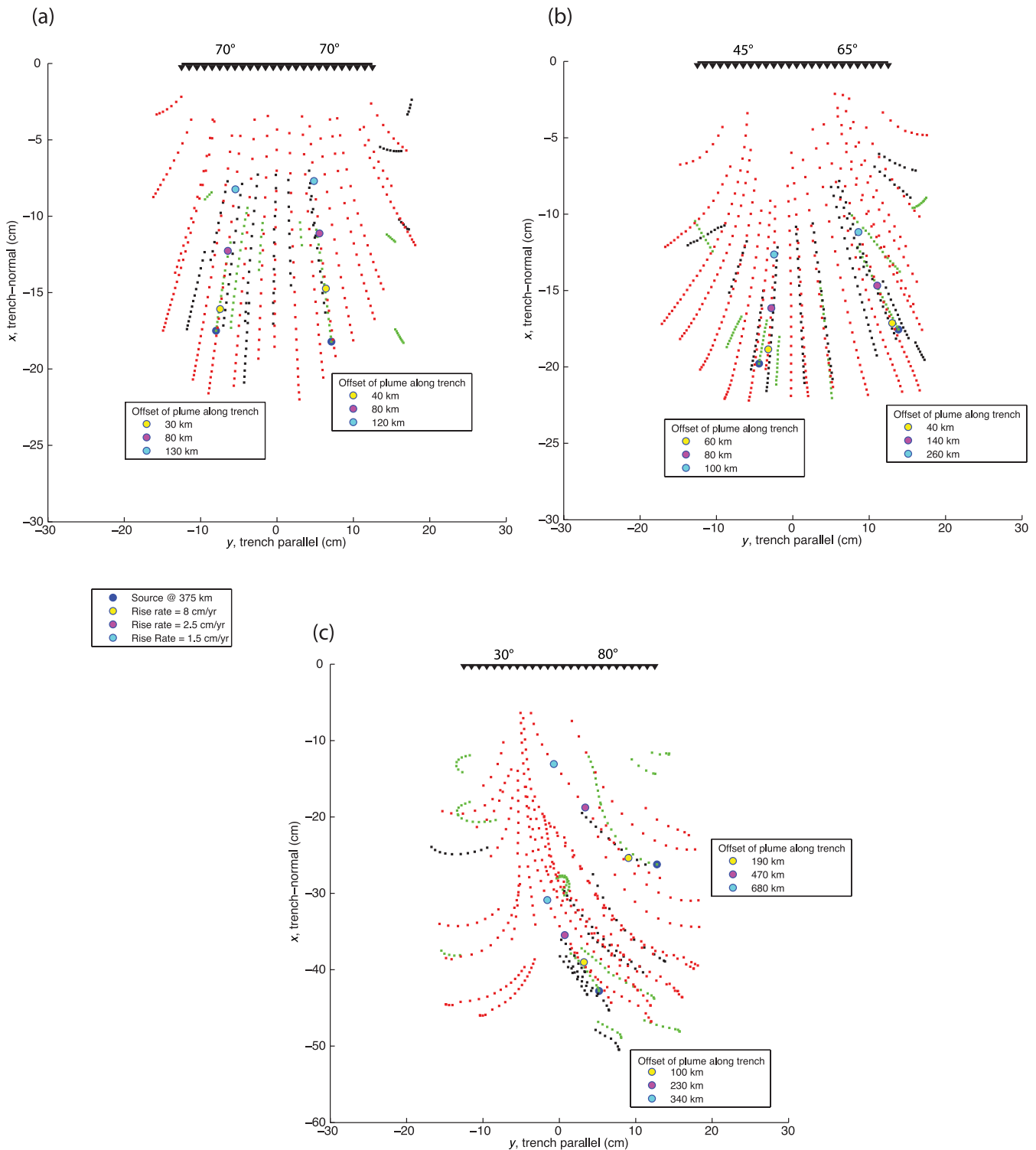
Figure 11. Estimates of diapir locations for (a) a constant, steep-dip slab (Exp. 3), (b) a small slab gap size with intermediate slab dips (Exp. 8) and (c) the maximum slab gap size and rollback (Exp. 16). The legend beneath (a) holds for all three figures. Based on the different rise rates, the diapirs are propagated along (close to) overlapping marker paths first in z3 (green points), then in z2 (black points), then in z1 (red points). The trench-parallel distance (i.e. in *y*) is calculated and translated into the real Earth system by our conversion of 1 cm in the lab equals 50 km in the Earth reference frame. Slab segment dip values are shown above their corresponding halves of the trench.

layer to the next (in this analysis, $n_{rise} = 1, 3$ or 5), q is the marker path at a given time step, q_h is the horizontal position of the diapir along that path line and o is the original time step of the marker located closest to the position of the diapir in the previous layer or

at the source. As seen in Fig. 11, we find that the trench-parallel (*y*-direction) offsets between the initial and final diapir locations are as small as ∼30 km in the constant-dip case with a steeply dipping slab (Fig. 11a), and as large as ∼680 km in the case with rollback

(Fig. 11c). We estimate uncertainties in these calculations to be ±20 km.

These results demonstrate that material path lines between the top of the subducting slab and surface volcanic centres are not directly vertical, and that trench-parallel offsets increase with greater subduction complexity, especially in the experiment with slab rollback. However, diapirs or fluids rising at rates much faster than the downdip subduction rate (not shown) would experience smaller offsets (i.e. have much more vertical paths) than those seen in Fig. 11 (Kincaid *et al.* 2013). These findings have implications for geochemical studies that look for melt signatures directly above (e.g. Smith & Price 2006) or directly trenchwards (e.g. Green & Harry 1999; Leeman *et al.* 2005; Pearce *et al.* 2005) of the hypothesized melting source on the subducting slab; these melt signatures may actually be found much closer to the slab centreline or on the shallowly dipping slab (if one is present) than their origin points alone suggest, especially when slab rollback or an unusual slab geometry is present. The flow fields strongly vary with changing dip values and the imposition of rollback; the response of vertically rising material through these flow fields is similarly complex.

Mantle anisotropy and shear wave splitting

To assess how the whisker azimuths observed in Exps 16/20 and 17 might translate into potential shear wave splitting in real subduction zones, shear wave splitting values were calculated by propagating synthetic local *s* and *SK(K)S* waves through an anisotropic model based on the observed whisker orientations. Although development of real olivine LPO and anisotropy in the mantle will no doubt differ in some respects from the simple whisker rotations (for example, the effects of recrystallization), these calculations provide a first-order estimate of the shear wave splitting implied by the experiments in this study.

Our model of anisotropy is divided into three layers in depth, each with a thickness of 125 km (including both the width of the light sheet and the gap above it to the next light sheet or to the surface of the fluid). Horizontal variation of anisotropy is specified by the whisker orientations of each block that falls within a given model layer (e.g. Figs 9 and 10). Elastic constants are specified by a blend of 70 per cent olivine (the averaged forsterite elastic constants of Anderson & Isaak (1995) and Abramson *et al.* (1997)) and 30 per cent orthopyroxene (the bronzite elastic constants of Frisillo & Barsch 1972). For each whisker in a block, these constants are rotated so that the olivine *a*-axis orientation is parallel to the whisker azimuth; aggregate block coefficients are the result of averaging over all of the rotated coefficients (i.e. whisker orientations) within the block. Whisker alignments observed on or near the shallow slab (z3 level) are subparallel to slab dip; we vertically rotate the averaged elastic constants for these whisker azimuths to match the 30° dip of the shallowly dipping slab. Elastic constants in the z2 and z1 layers are left horizontal; the whiskers at these depths do not show strong enough downdip alignment to warrant a vertical rotation.

Once the elastic constants for a model block are calculated, we determine the ray path through each model block. To model splitting for local *s* waves from intermediate depth earthquakes, we propagate synthetic local *s* waves through only the upper two depth slices (from 250 to 0 km depth; Fig. 10). Assuming an initial incidence angle of 30° in the z2 layer, we calculate the incidence angle in the z1 layer that would conserve phase ray parameter, assuming that the phase propagates at the average of the fast and slow shear wave velocities. Ray paths are determined in a similar manner for the synthetic

SK(K)S waves, except that all three layers are included (Fig. 10), and the initial incidence angle of the *SK(K)S* wave in the z3 layer is 15°. Local *s* and *SK(K)S* ray paths are calculated over a range of backazimuths from 0° to 180° (with respect to the orientation of the trench).

Splitting is predicted for local *S* and *SK(K)S* waves with periods of roughly 2 and 10 s, respectively. As *SKS* and *SKKS* waves emerge from the core as purely *SV* motion, the initial 10-s Gaussian wavelet for these phases is polarized in the plane of the phase path. The initial 2-s Gaussian wavelets for the local *s* phases are assigned equal *SV* and *SH* motion. For the incidence angle and backazimuth in each layer, the Christoffel equation is used to determine the particle motion and phase velocities of the fast and slow shear waves. For each layer, the wavelet is rotated into the fast and slow shear wave polarizations, the fast and slow polarizations are offset by the shear wave splitting time for the layer and the phase is then rotated back into its original coordinate system. Using the particle motions calculated at the surface, which integrate the effects of anisotropy in all layers, shear wave splitting parameters (fast direction, φ, and splitting time, d*t*) are calculated using the eigenvalue minimization of Silver & Chan (1991).

The strength of anisotropy is adjusted to match the estimate of splitting time per kilometre of mantle wedge (2.2×10^{-3} s km^{-1}) calculated for the South American subduction zone by MacDougall *et al.* (2012). Anisotropic strength is reduced from single crystal values by applying a uniform dilution factor (i.e. the anisotropy percentage) to the elastic coefficients for each whisker. This assumption produces backazimuth-averaged splitting times of 0.66–0.67 s for the *SK(K)S* waves and 0.38–0.39 s for the local *s* waves. Averaged predicted shear wave splitting parameters for local *s* and *SK(K)S* phases in model blocks 10 and 14 for Exps 16/20 and 17 are given in Fig. 10. The predicted splitting values, as a function of backazimuth, are in Table S1.

Predicted shear wave splitting fast polarizations for model blocks 10 and 14 in Exps 16/20 and 17 yield averages that range from mildly (−10°) to moderately (−30°) deflected from trench-normal, respectively. In the backarc (block 10) of both experiments, whisker orientation rose diagrams show little variation in depth (Fig. 10); averaged predicted local *s* and *SK(K)S* shear wave splitting fast polarizations are close to the mean whisker orientations observed in each model layer and range from −10° to −15° (Fig. 10). At the slab gap in the case without rollback (block 14, Exp. 17), however, trench-parallel flow near the slab gap causes average whisker azimuths to be rotated counter-clockwise in depth (Figs 9 and 10); averaged predicted local *s* and *SK(K)S* fast directions for this case are −29° and −33°, respectively. In comparison, rollback counteracts much of the trench-parallel flow produced by the slab gap (block 14, Exp. 16/20), yielding more trench-normal averaged fast polarizations of −12° and −15°.

While some portions of the mantle wedge near the slab gap manifest trench-parallel flow and whisker alignments indicative of the 'trench-parallel stretching' modelled by Kneller & van Keken (2007), none of these flow fields produce trench-parallel whisker alignments over a large enough depth range to generate trench-parallel shear wave splitting fast polarizations. Thus the flow patterns in these experiments do not explain the trench-parallel fast polarizations observed in many subduction zones, including those from local *s* phases representing anisotropy within the mantle wedge (e.g. Yang *et al.* 1995; Fouch & Fischer 1996; Audoine *et al.* 2000; Polet *et al.* 2000; Anderson *et al.* 2005; Long & van der Hilst 2006; Long & Silver 2008; Abt *et al.* 2009; MacDougall *et al.* 2012; Long 2013). This result raises several possibilities: (1) other geodynamic

factors may be at work (resulting in different shear patterns), (2) factors other than those represented by whiskers control olivine *a*-axis orientations (i.e. dynamic recrystallization, non A-type olivine, etc.) or (3) other mineralogies or sources of anisotropy (e.g. melt) strongly influence the anisotropy observed in subduction zones.

Comprehensively considering all alternative possibilities to explain trench-parallel shear wave splitting fast polarizations goes well beyond the scope of this study, but a few may be relatively easily evaluated, including anisotropy in the subducting slab and the presence of B-type olivine fabric in the mantle wedge. While anisotropy within the subducting slab may be present and can produce significant shear wave splitting (e.g. Faccenda *et al.* 2008; Healy *et al.* 2009; Hammond *et al.* 2010), these effects will be the largest at forearc stations, where phase path lengths through the slab can be longer than those that sample the mantle wedge. With B-type olivine fabrics, the olivine *a*-axis aligns perpendicular to the flow direction; trench-normal flow in the mantle wedge would produce trench-parallel shear wave splitting observations at the surface (e.g. Jung & Karato 2001). However, B-type olivine is generated in water-rich, high stress, low-temperature environments (Jung & Karato 2001; Jung *et al.* 2006; Katayama & Karato 2006); numerical modelling indicates that these conditions only occur in the forearc of the mantle wedge (Kneller *et al.* 2005; Kneller *et al.* 2007). Thus neither slab anisotropy nor B-type fabrics provide sufficient explanations for the abundant trench-parallel fast directions from local *s* paths that sample the hotter regions of the mantle wedge beneath arc and backarc regions of many subduction zones.

The influence of slab rollback is a key issue in the interpretation of seismic anisotropy in subduction zones. Slab rollback has long been invoked to explain observed trench-parallel fast polarizations from *SK(K)S* phases that sample anisotropy below the slab (e.g. Russo & Silver 1994), and experimental and numerical studies have shown that rollback has the potential to produce a zone of trench-parallel olivine *a*-axes below the slab (e.g. Buttles & Olson 1998; Kincaid & Griffiths 2003; Kincaid & Griffiths 2004; Schellart 2004; Funiciello *et al.* 2006; Jadamec & Billen 2010, 2012; Faccenda & Capitanio 2013). Rollback has also been thought to drive flow that would create olivine alignments consistent with trench-parallel splitting fast polarizations within the mantle wedge (e.g. Long & Silver 2008; Abt *et al.* 2009). However, recent experimental and numerical models (including this one) have shown that rollback will instead tend to produce trench-normal olivine *a*-axes above central regions of the slab away from toroidal flow around slab edges (Druken *et al.* 2011; Faccenda & Capitanio 2012, 2013). We observe that rollback modifies flow patterns so that trench-normal flow at least partially erases trench-parallel flow near the slab gap. However, whisker alignments in our experiment with rollback are also not purely trench-normal, indicating that the interaction of slab gaps and rollback can produce a range of olivine *a*-axis orientations that vary on small length scales, as has been observed in some subduction zone segments (e.g. MacDougall *et al.* 2012).

CONCLUSIONS

Our laboratory experiments exhibit time varying, 3-D circulation patterns in response to different styles of subduction with complex plate geometries. In our reference cases, which have a constant slab dip value, flow in the mantle wedge is roughly symmetric about the slab centreline. Marker speeds increase with larger dip angles, as does the two-dimensionality of the path lines. 3-D flow is more obvious at shallower dip angles, where path lines have increasingly trench-oblique to trench-parallel orientations.

Slab dip variations generate even greater 3-D flow in the wedge; trench-parallel flow perturbs path lines from above the steeper slab towards the forearc above the shallower slab. This flow is consistent with analytical (Hall *et al.* 2000) and numerical (Kneller & van Keken 2007, 2008) models that indicate the same sense of flow produced by reduced pressures above the shallowly dipping slab. The rate of trench-parallel flow increases with the magnitude of the trench-parallel slab dip variation, and, for a fixed slab dip difference, as the dip of the shallowly dipping slab segment decreases. Total flow rates also increase with slab dip difference.

Rollback enhances flow rates in all regions of the wedge, particularly in the region above the steeper plate. Rollback in the presence of a slab gap also tends to enhance trench-parallel flow across the slab centreline, and results in stronger penetration of subslab mantle into the wedge. In our models, this through-flow is largely horizontal, and is therefore not expected to passively or actively feed into decompression melting.

These results also allow us to draw conclusions about arc melt paths and mantle wedge seismic anisotropy. Path line asymmetry in cases with complex slab morphology produces significant spatial offsets between the deep source location and the near-surface delivery of arc melts. Despite causing trench-parallel or trench-oblique path line deflections, near the slab gap rollback produces trench-normal whiskers alignments that counter the tendency of the slab dip change to drive whisker rotation towards the shallowly dipping slab. The production of trench-parallel flow due to subduction of a slab gap causes whisker rotations near the slab gap of up to 30° away from trench-normal. Rollback drives whisker rotation near the slab gap into orientations that are only 10° away from trench-normal.

These experiments show that a slab gap can generate significant perturbations in wedge flow and both seismic and geochemical signals recorded at the surface in convergent margins. However, even in cases that maximize the amount of trench-parallel wedge flow (no rollback, large slab gap with one very shallowly dipping slab), whiskers in the central mantle wedge never become strongly aligned in the trench-parallel direction. While slab anisotropy and B-type olivine fabric may contribute to trench-parallel shear wave splitting observations in the forearc, other mechanisms are still needed to explain the extensive zones of trench-parallel shear wave splitting fast polarizations observed in the arc and backarc regions of many subduction zones.

ACKNOWLEDGEMENTS

REFERENCES

Abramson, E.H., Brown, J.M., Slutsky, L.J. & Zaug, J., 1997. The elastic constants of San Carlos olivine to 17 GPa, *J. geophys. Res.,* **102,** 12 253–12 263.

Abratis, M. & Worner, G., 2001. Ridge collision, slab-window formation, and the flux of Pacific asthenosphere into the Caribbean realm, *Geology,* **29,** 127–130.

Abt, D. L., Fischer, K.M., Abers, G.A., Strauch, W., Protti, J.M. & González, V., 2009. Shear wave anisotropy beneath Nicaragua and Costa Rica: implications for flow in the mantle wedge, *Geochem. Geophys. Geosyst.,* **10,** Q05S15, doi:10.1029/2009GC002375.

Abt, D. L., Fischer, K.M., Abers, G.A., Protti, M., Gonzalez, V. & Strauch, W., 2010. Constraints on upper mantle anisotropy surrounding the Cocos slab from SK(K)S splitting, *J. geophys. Res.,* **115,** B06316, doi:10.1029/2009JB006710.

Anderson, M.L., Zandt, G., Triep, E., Fouch, M. & Beck, S., 2004. Anisotropy and mantle flow in the Chile-Argentina subduction zone from shear wave splitting analysis, *Geophys. Res. Lett.,* **31,** L23608, doi:10.1029/2004GL020906.

Anderson, M.L., Wagner, L., Gilbert, H., Alvarado, P., Zandt, G., Beck, S. & Triep, E., 2005. Constraints on mantle kinematics influenced by a changing slab geometry: results from the CHARGE project, in *Proceedings of South America, IASPEI General Assembly,* Santiago, Chile, October, Abstract # 1000.

Anderson, O.L. & Isaak, D.G., 1995. Elastic constants of mantle minerals at high temperature, in *Mineral Physics and Crystallography: A Handbook of Physical Constants, AGU Ref. Shelf,* Vol. **2,** pp. 64–97, ed. Aherns, T.J., AGU.

Audoine, E., Savage, M.K. & Gledhill, K., 2000. Seismic anisotropy from local earthquakes in the transition region from a subduction to a strike-slip plate boundary, New Zealand, *J. geophys. Res.,* **105,** 8013–8033.

Baccheschi, P., Margheriti, L. & Steckler, M.S., 2007. Seismic anisotropy reveals focused mantle flow around the Calabrian slab (Southern Italy), *Geophys. Res. Lett.,* **34,** L05302, doi:10.1029/2006GL028899.

Becker, T.W. & Faccenna, C., 2009. A review of the role of subduction for regional and global plate motions, in *Subduction Zone Geodynamics,* pp. 3–34, eds Lallemand, S. & Funiciello, F., Springer-Verlag.

Behn, M.D., Hirth, G. & Kelemen, P.B. 2007. Trench-parallel anisotropy produced by foundering of arc crust, *Science,* **317,** 108–111.

Billen, M.I. & Jadamec, M., 2012. Origin of localized fast mantle flow velocity in numerical models of subduction, *Geochem. Geophys. Geosyst.,* **13,** Q01016, doi:10.1029/2011GC003856.

Buttles, J. & Olson, P., 1998. A laboratory model of subduction zone anisotropy, *Earth planet. Sci. Lett.,* **164,** 245–262.

Christensen, D.H. & Abers, G.A., 2010. Seismic anisotropy under central Alaska from SKS splitting observations, *J. geophys. Res.,* **115,** B04315, doi:10.1029/2009JB006712.

Civello, S. & Margheriti, L., 2004. Toroidal mantle flow around the Calabrian slab (Italy) from SKS splitting, *Geophys. Res. Lett.,* **31,** L10601, doi:10.1029/2004GL019607.

Conder, J.A., Wiens, D.A. & Morris, J., 2002. On the decompression melting structure at volcanic arcs and back-arc spreading centers, *Geophys. Res. Lett.,* **29,** 17-1–17-4.

Davies, G.F., 1977. Viscous mantle flow under moving lithospheric plates and under subduction zones, *Geophys. J. Int.,* **49,** 557–563.

D'Orazio, M., Agostini, S., Mazzarini, F., Innocenti, F., Manetti, P., Haller, M.J. & Lahsen, A., 2000. The Pali Aike volcanic field, Patagonia: slab-window magmatism near the tip of South America, *Tectonophysics,* **321,** 407–427.

Druken, K.A., Long, M.D. & Kincaid, C., 2011. Patterns in seismic anisotropy driven by rollback subduction beneath the High Lava Plains, *Geophys. Res. Lett.,* **38,** L13310, doi:10.1029/2011GL047541.

Druken, K.A., Kincaid, C. & Griffiths, R.W., 2013. Directions of seismic anisotropy in laboratory models of mantle plumes, *Geophys. Res. Lett.,* **40,** 3544–3549.

Escrig, S., Bézos, A., Goldstein, S.L., Langmuir, C.H. & Michael, P.J., 2009. Mantle source variations beneath the Eastern Lau Spreading Center and the nature of subduction components in the Lau Basin-Tonga arc system, *Geochem. Geophys. Geosyst.,* **10,** Q04014, doi:10.1029/2008GC002281.

Faccenda, M. & Capitanio, F.A., 2012. Development of mantle seismic anisotropy during subduction-induced 3-D flow, *Geophys. Res. Lett.,* **39,** L11305, doi:10.1029/2012GL051988.

Faccenda, M. & Capitanio, F.A., 2013. Seismic anisotropy around subduction zones: insights from three-dimensional modeling of upper mantle deformation and SKS splitting calculations, *Geochem. Geophys. Geosyst.,* **14,** 243–262.

Faccenda, M., Burlini, L., Gerya, T.V. & Mainprice, D., 2008. Fault-induced seismic anisotropy by hydration in subducting oceanic plates, *Nature,* **455,** 1097–1100.

Faccenna, C., Civetta, L., D'Antonio, M., Funiciello, F., Margheriti, L. & Piromallo, C., 2005. Constraints on mantle circulation around the deforming Calabrian slab, *Geophys. Res. Lett.,* **32,** L06311, doi:10.1029/2004GL021874.

Falloon, T.J. *et al.*, 2007. Multiple mantle plume components involved in the petrogenesis of subduction-related lavas from the northern termination of the Tonga Arc and northern Lau Basin: evidence from the geochemistry of arc and backarc submarine volcanoes, *Geochem. Geophys. Geosyst.,* **8,** Q09003, doi:10.1029/2007GC001619.

Ferrari, L., 2004. Slab detachment control on mafic volcanic pulse and mantle heterogeneity in central Mexico, *Geology,* **32,** 77–80.

Fouch, M.J. & Fischer, K.M., 1996. Mantle anisotropy beneath northwest Pacific subduction zones, *J. geophys. Res.,* **101,** 15 987–16 002.

Frisillo, A.L. & Barsch, G.R., 1972. Measurement of single-crystal elastic constants of bronzite as a function of pressure and temperature, *J. geophys. Res.,* **77,** 6360–6384.

Funiciello, F., Faccenna, C., Giardini, D. & Regenauer-Lieb, K., 2003. Dynamics of retreating slabs: 2. Insights from three-dimensional laboratory experiments, *J. geophys. Res.,* **108**(B4), 2207, doi:10.1029/2001JB000896.

Funiciello, F., Moroni, M., Piromallo, C., Faccenna, C., Cenedese, A. & Bui, H.A., 2006. Mapping mantle flow during retreating subduction: laboratory models analyzed by feature tracking, *J. geophys. Res.,* **111,** B03402, doi:10.1029/2005JB003792.

Garfunkel, Z., Anderson, C.A. & Schubert, G., 1986. Mantle circulation and the lateral migration of subducted slabs, *J. geophys. Res.,* **91,** 7205–7223.

Gazel, E. *et al.*, 2011. Plume-subduction interaction in southern Central America: mantle upwelling and slab melting, *Lithos,* **121,** 117–134.

Gerya, T.V. & Yuen, D.A., 2003. Rayleigh-Taylor instabilities from hydration and melting propel 'cold plumes' at subduction zones, *Earth planet. Sci. Lett.,* **212,** 47–62.

Gerya, T.V., Yuen, D.A. & Sevre, E.O.D., 2004. Dynamical causes for incipient magma chambers above slabs, *Geology,* **32,** 89–92.

Green, N.L. & Harry, D.L., 1999. On the relationship between subducted slab age and arc basalt petrogenesis, Cascadia subduction system, North America, *Earth planet. Sci. Lett.,* **171,** 367–381.

Griffiths, R.W., Hackney, R.I. & van der Hilst, R.D., 1995. A laboratory investigation of effects of trench migration on the descent of subducted slabs, *Earth planet. Sci. Lett.,* **133,** 1–17.

Guivel, C. *et al.*, 2006. Miocene to Late Quaternary Patagonian basalts (46–47°S): geochronometric and geochemical evidence for slab tearing due to active spreading ridge subduction, *J. Volc. Geotherm. Res.,* **149,** 346–370.

Guo, L., Zhang, H.-F., Harris, N., Pan, F.-B. & Xu, W.-C., 2011. Origin and evolution of multi-stage felsic melts in eastern Gangdese belt: constraints from U-Pb zircon dating and Hf isotopic composition, *Lithos,* **127,** 54–67.

Gutiérrez, F., Gioncada, A., González Ferran, O., Lahsen, A. & Mazzuoli, R., 2005. The Hudson Volcano and surrounding monogenetic centres (Chilean Patagonia): an example of volcanism associated with ridge-trench collision environment, *J. Volc. Geotherm. Res.,* **145,** 207–233.

Hall, C.E., Fischer, K.M., Parmentier, E.M. & Blackman, D.K., 2000. The influence of plate motions on three-dimensional back arc mantle flow and shear wave splitting, *J. geophys. Res.,* **105,** 28 009–28 033.

Hall, P.S. & Kincaid, C., 2001. Diapiric flow at subduction zones: a recipe for rapid transport, *Science,* **292,** 2472–2475.

Hammond, J.O.S., Wookey, J., Kaneshima, S., Inoue, H., Yamashina, T. & Harjadi, P., 2010. Systematic variation in anisotropy beneath the mantle wedge in the Java-Sumatra subduction system from shear-wave splitting, *Phys. Earth planet. Inter.,* **178,** 189–201.

Hart, S.R., Coetzee, M., Workman, R.K., Blusztajn, J., Johnson, K.T.M., Sinton, J.M., Steinberger, B. & Hawkins, J.W., 2004, Genesis of Western Samoa seamount province: age, geochemical fingerprint and tectonics, *Earth planet. Sci. Lett.,* **227,** 37–56.

Hasenclever, J., Morgan, J.P., Hort, M. & Rüpke, L.H., 2011. 2D and 3D numerical models on compositionally buoyant diapirs in the mantle wedge, *Earth planet. Sci. Lett.,* **311,** 53–68.

Healy, D., Reddy, S.M., Timms, N.E., Gray, E.M. & Brovarone, A.V., 2009. Trench-parallel fast axes of seismic anisotropy due to fluid-filled cracks in subducting slabs, *Earth planet. Sci. Lett.,* **283,** 75–86.

Herrstrom, E.A., Reagan, M.K. & Morris, J.D., 1995. Variations in lava composition associated with flow of asthenosphere beneath southern Central America, *Geology,* **23,** 617–620.

Hicks, S.P, Nippress, S.E.J. & Rietbrock, A., 2012. Sub-slab mantle anisotropy beneath south-central Chile, *Earth planet. Sci. Lett.,* **357–358,** 203–213.

Hoernle, K. *et al.*, 2008. Arc-parallel flow in the mantle wedge beneath Costa Rica and Nicaragua, *Nature,* **451,** 1094–1097.

Honda, S., 2008. A simple semi-dynamic model of the subduction zone: effects of a moving plate boundary on the small-scale convection under the island arc, *Geophys. J. Int.,* **173,** 1095–1105.

Honda, S., 2009. Numerical simulations of mantle flow around slab edges, *Earth planet. Sci. Lett.,* **277,** 112–122.

Jadamec, M.A. & Billen, M.I., 2010, Reconciling surface plate motions with rapid three-dimensional mantle flow around a slab edge, *Nature,* **465,** 338–441.

Jadamec, M.A. & Billen, M.I., 2012. The role of rheology and slab shape on rapid mantle flow: three-dimensional numerical models of the Alaska slab edge, *J. geophys. Res.,* **117,** B02304, doi:10.1029/2011JB008563.

Jeffery, G., 1922. The motion of ellipsoidal particles immersed in a viscous fluid, *Proc. R. Soc. Lond.,* **102,** 161–179.

Jung, H., 2011. Seismic anisotropy produced by serpentine in the mantle wedge, *Earth planet. Sci. Lett.,* **307,** 535–543.

Jung, H. & Karato, S.-I., 2001. Water-induced fabric transitions in olivine, *Science,* **293,** 1460–1463.

Jung, H., Katayama, I., Jiang, Z., Hiraga, T. & Karato, S.-I., 2006. Effect of water and stress on the lattice-preferred orientation of olivine, *Tectonophysics,* **421,** 1–22.

Karato, S.-I., Jung, H., Katayama, I. & Skemer, P., 2008. Geodynamic significance of the seismic anisotropy of the upper mantle: new insights from laboratory studies, *Annu. Rev. Earth planet. Sci. Lett.,* **36,** 59–95.

Karsten, J.L., Klein, E.M. & Sherman, S.B., 1996. Subduction zone geochemical characteristics in ocean ridge basalts from southern Chile Ridge: implications of modern ridge subduction systems for the Archean, *Lithos,* **37,** 143–161.

Katayama, I. & Karato, S.-I., 2006. Effect of temperature on the B- to C-type olivine fabric transition and implication for flow pattern in subduction zones, *Phys. Earth. planet. Inter.,* **157,** 33–45.

Katayama, I., Hirauchi, K.-i., Michibayashi, K. & Ando, J.-i., 2009. Trench-parallel anisotropy produced by serpentine deformation in the hydrated mantle wedge, *Nature,* **461,** 1114–1117.

Kelemen, P.B., Rilling, J.L., Parmentier, E.M., Mehl, L. & Hacker, B.R., 2003. Thermal structure due to solid-state flow in the mantle wedge beneath arcs, in *Inside the Subduction Factory*, *Geophysical Monograph Series,* Vol. **138,** pp. 293–311, ed. Eiler, J.M., AGU.

Kincaid, C. & Griffiths, R.W., 2003. Laboratory models of the thermal evolution of the mantle during rollback subduction, *Nature,* **425,** 58–62.

Kincaid, C. & Griffiths, R.W., 2004. Variability in flow and temperatures within mantle subduction zones, *Geochem. Geophys. Geosyst.,* **5,** Q06002, doi:10.1029/2003GC000666.

Kincaid, C. & Hall, P.S., 2003. Role of back arc spreading in circulation and melting at subduction zones, *J. geophys. Res.,* **108,** 2240, doi:10.1029/2001JB001174.

Kincaid, C. & Olson, P., 1987. An experimental study of subduction and slab migration, *J. geophys. Res.,* **92,** 13 832–13 840.

Kincaid, C. & Sacks, I.S., 1997. Thermal and dynamical evolution of the upper mantle in subduction zones, *J. geophys. Res.,* **102,** 12 295–12 315.

Kincaid, C., Druken, K.A., Griffiths, R.W. & Stegman, D. R., 2013. Bifurcation of the Yellowstone plume driven by subduction-induced mantle flow, *Nature Geosci.,* **6,** 395–399.

Klein, E.M. & Karsten, J.L., 1995. Ocean-ridge basalts with convergent-margin geochemical affinities from the Chile Ridge, *Nature,* **374,** 52–57.

Kneller, E.A. & van Keken, P.E., 2007. Trench-parallel flow and seismic anisotropy in the Mariana and Andean subduction systems, *Nature,* **450,** 1222–1225.

Kneller, E.A. & van Keken, P.E., 2008. Effect of three-dimensional slab geometry on deformation in the mantle wedge: implications for shear wave anisotropy, *Geochem. Geophys. Geosyst.,* **9,** Q01003, doi:10.1029/2007GC001677.

Kneller, E.A., van Keken, P.E., Karato, S.-I. & Park, J., 2005. B-type olivine fabric in the mantle wedge: insights from high-resolution non-Newtonian subduction zone models, *Earth. planet. Sci. Lett.,* **237,** 781–797.

Kneller, E.A., van Keken, P.E., Katayama, I. & Karato, S.-I., 2007. Stress, strain, and B-type olivine fabric in the fore-arc mantle: sensitivity tests using high-resolution steady-state subduction zone models, *J. geophys. Res.,* **112,** B04406, doi:10.1029/2006JB004544.

Lassak, T.M., Fouch, M.J., Hall, C.E. & Kaminski, E., 2006. Seismic characterization of mantle flow in subduction systems: can we resolve a hydrated mantle wedge? *Earth planet. Sci. Lett.,* **243,** 632–649.

Leeman, W.P., Lewis, J.F., Evarts, R.C., Conrey, R.M. & Streck, M.J., 2005. Petrologic constraints on the thermal structure of the Cascades arc, *J. Volc. Geotherm. Res.,* **140,** 67–105.

Lev, E. & Hager, B.H., 2011. Anisotropy viscosity changes subduction zone thermal structure, *Geochem. Geophys. Geosyst.,* **12,** Q04009, doi:10.1029/2010GC003382.

Levin, V., Droznin, D., Park, J. & Gordeev, E., 2004. Detailed mapping of seismic anisotropy with local shear waves in southeastern Kamchatka, *Geophys. J. Int.,* **158,** 1009–1023.

Li, Z.-H. & Ribe, N.M., 2012. Dynamics of free subduction from 3D boundary element modeling, *J. geophys. Res.,* **117,** B06408, doi:10.1029/2012JB009165.

Long, M.D., 2013. Constraints on subduction geodynamics from seismic anisotropy, *Rev. Geophys.,* **51,** 76–112.

Long, M.D. & van der Hilst, R.D., 2006. Shear wave splitting from local events beneath the Ryukyu arc: trench-parallel anisotropy in the mantle wedge, *Phys. Earth planet. Inter.,* **155,** 300–312.

Long, M.D. & Silver, P.G., 2008. The subduction zone flow field from seismic anisotropy: a global view, *Science,* **319,** 315–318.

MacDougall, J.G., Fischer, K.M. & Anderson, M.L., 2012. Seismic anisotropy above and below the subducting Nazca lithosphere in southern South America, *J. geophys. Res.,* **117,** B12306, doi:10.1029/2012JB009538.

Macera, P., Gasperini, D., Ranalli, G. & Mahatsente, R., 2008. Slab detachment and mantle plume upwelling in subduction zones: an example from the Italian South-Eastern Alps, *J. Geodyn.,* **45,** 32–48.

Matcham, I., Savage, M.K. & Gledhill, K.R., 2000. Distribution of seismic anisotropy in the subduction zone beneath the Wellington region, New Zealand, *Geophys. J. Int.,* **140,** 1–10.

Pan, F.-B., Zhang, H.-F., Harris, N., Xu, W.-C. & Guo, L., 2012. Oligocene magmatism in the eastern margin of the east Himalayan syntaxis and its implications for the India-Asia post-collisional process, *Lithos,* **154,** 181–192.

Peacock, S. M., 1996. Thermal and petrologic structure of subduction zones, in *Subduction Top to Bottom*, *Geophysical Monograph Series,* Vol. **96,** pp. 119–133, eds Bebout, G.E., Scholl, D.W., Kirby, S.H. & Platt, J.P., AGU.

Peacock, S. M., 2003. Thermal structure and metamorphic evolution of subducting slabs, in *Inside the Subduction Factory*, *Geophysical Monograph Series,* Vol. **138,** pp. 7–22, ed. Eiler, J.M., AGU.

Pearce, J.A., Stern, R.J., Bloomer, S.H. & Fryer, P., 2005. Geochemical mapping of the Mariana arc-basin system: implications for the nature and distribution of subduction components, *Geochem. Geophys. Geosyst.,* **6,** Q07006, doi:10.1029/2004GC000895.

Peyton, V., Levin, V., Park, J., Brandon, M., Lees, J., Gordeev, E. & Ozerov, A., 2001. Mantle flow at a slab edge: seismic anisotropy in the Kamchatka region, *Geophys. Res. Lett.,* **28,** 379–382.

Piromallo, C., Becker, T.W., Funiciello, F. & Faccenna, C., 2006. Three-dimensional instantaneous mantle flow induced by subduction, *Geophys. Res. Lett.,* **33,** L08304, doi:10.1029/2005GL025390.

Polet, J., Silver, P.G., Beck, S., Wallace, T., Zandt, G., Ruppert, S., Kind, R. & Rudloff, A., 2000. Shear wave anisotropy beneath the Andes from the BANJO, SEDA, and PISCO experiments, *J. geophys. Res.,* **105,** 6287–6304.

Regelous, M., Turner, S., Falloon, T.J., Taylor, P., Gamble, J. & Green, T., 2008. Mantle dynamics and mantle melting beneath Niuafo'ou Island and the northern Lau back-arc basin, *Contrib. Mineral. Petrol.,* **156,** 103–118.

Ribe, N.M., 1989a. Seismic anisotropy and mantle flow, *J. geophys. Res.,* **94,** 4213–4223.

Ribe, N.M., 1989b. A continuum theory for lattice preferred orientation, *Geophys. J. Int.,* **97,** 199–207.

Russo, R.M. & Silver, P.G., 1994. Trench-parallel flow beneath the Nazca Plate from seismic anisotropy, *Science,* **263,** 1105–1111.

Russo, R.M., Gallego, A., Comte, D., Mocanu, V.I., Murdie, R.E. & VanDecar, J.C., 2010. Source-side shear wave splitting and upper mantle flow in the Chile Ridge subduction region, *Geology,* **38,** 707–710.

Schellart, W.P., 2004. Kinematics of subduction and subduction-induced flow in the upper mantle, *J. geophys. Res.,* **109,** B07401, doi:10.1029/2004JB002970.

Schellart, W.P., Freeman, J., Stegman, D.R., Moresi, L. & May, D., 2007. Evolution and diversity of subduction zones controlled by slab width, *Nature,* **446,** 308–311.

Schellart, W.P., Stegman, D.R., Farrington, R.J. & Moresi, L., 2011. Influence of lateral slab edge distance on plate velocity, trench velocity, and subduction partitioning, *J. geophys. Res.,* **116,** B10408, doi:10.1029/2011JB008535.

Silver, P.G. & Chan, W.W., 1991. Shear wave splitting and subcontinental mantle deformation, *J. geophys. Res.,* **96,** 16 429–16 454.

Smith, G.P., Wiens, D.A., Fischer, K.M., Dorman, L.M., Webb, S.C. & Hildebrand, J.A., 2001. A complex pattern of mantle flow in the Lau Backarc, *Science,* **292,** 713–716.

Smith, I.E.M. & Price, R.C., 2006. The Tonga-Kermadec arc and Havre-Lau back-arc system: their role in the development of tectonic and magmatic models for the western Pacific, *J. Volc. Geotherm. Res.,* **156,** 315–331.

Syracuse, E.M., van Keken, P.E. & Abers, G.A., 2010. The global range of subduction zone thermal models, *Phys. Earth planet. Inter.,* **183,** 73–90.

Tovish, A., Schubert, G. & Luyendyk, B.P., 1978. Mantle flow pressure and the angle of subduction: non-Newtonian corner flows, *J. geophys. Res.,* **83,** 5892–5898.

Turcotte, D.L. & Schubert, G., 2002. *Geodynamics,* 2nd edn, pp. 242–244, Cambridge Univ. Press.

Turner, S. & Hawkesworth, C., 1998. Using geochemistry to map mantle flow beneath the Lau Basin, *Geology,* **26,** 1019–1022.

van Keken, P.E., Kiefer, B. & Peacock, S.M., 2002. High-resolution models of subduction zones: implications for mineral dehydration reactions and the transport of water into the deep mantle, *Geochem. Geophys. Geosyst.,* **3,** 1056, doi: 10.1029/2001GC000256.

Wendt, J.I., Regelous, M., Collerson, K.D. & Ewart, A., 1997. Evidence for a contribution from two mantle plumes to island arc lavas from northern Tonga, *Geology,* **25,** 611–614.

Yang, X., Fischer, K.M. & Abers, G.A., 1995. Seismic anisotropy beneath the Shumagin Islands segment of the Aleutian-Alaska subduction zone, *J. geophys. Res.,* **100,** 18 165–18 177.

Zhu, G., Gerya, T.V., Yuen, D.A., Honda, S., Yoshida, T. & Connolly, J.A.D., 2009. Three-dimensional dynamics of hydrous thermal-chemical plumes in oceanic subduction zones, *Geochem. Geophys. Geosyst.,* **10,** Q11006, doi:10.1029/2009GC002625.

APPENDIX

A.1 Additional analyses of u^*, $u_\perp^*$, u_{ll}^* and A_{norm}

These figures show u^*, $u_\perp^*$, u_{ll}^* *and* A_{norm} as a function of normalized distance from the trench (s_{norm}) for selected path line plots from Exps 3, 4, 7, 10 and 16. Fig. A1 is the expanded version of Figs 2(c)–(d), Fig. A2 is the expanded version of Figs 4(a) and (b) and Fig. A3 is the expanded version of Figs 6(a) and (b). A summary of the maximum u^* values for the z1 level of each experiment is shown in Fig. A4.

A.2 2-D corner flow solutions

Using the methods described in Hall *et al.* (2000) and Turcotte and Schubert (2002), we calculate 2-D pressure, pressure gradient and velocity values for slab dips of 30° and 60° (Fig. A5), using the material properties of the glucose syrup. With a smaller slab dip, non-hydrostatic pressures in the mantle wedge are more negative (Fig. A5, top row), and non-hydrostatic pressure gradients are larger (Fig. A5, middle row). These conditions cause stronger and more rapid wedge flow towards the shallowly dipping slab and away from the steeply dipping slab.

A.3 Flow and volume flux estimates through the slab gap

A path similar to the blue path in Fig. 7 is highlighted in Fig. A6(a), where a tracer starts out beneath the shallowly dipping slab, moves into the plane of the figure and enters the wedge above the steeply dipping slab, eventually subducting after 7 min of transport. Fig. A6(b) represents faster gap through-flow in the presence of slab rollback.

To obtain order-of-magnitude estimates for volume flux through a slab gap, we assume perfectly horizontal flow across a cross-section whose width equals the separation of the two belts measured in the trench-parallel direction, and whose triangular, cross-sectional shape is the one prescribed by the difference in dip between the slabs, down to the roller at 670 km ($D_{\text{L}} = 14$ cm; the area between the green line and the blue line in Figs A6(a) and (b). These volume flux estimates are therefore maximum possible values.
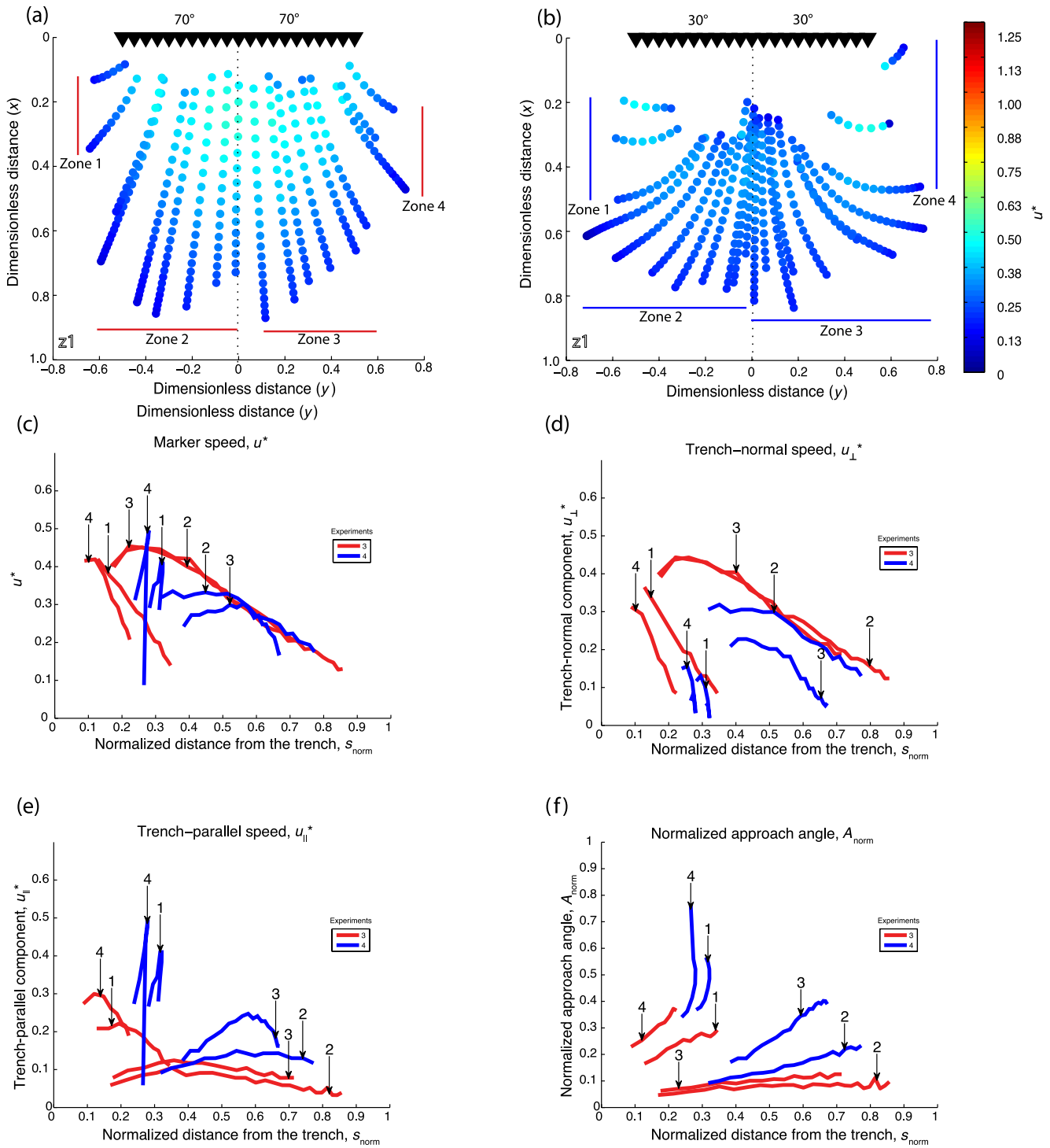
Figure A1. Comparison of Exps 3 ($U_D = 8\,\mathrm{cm\,min}^{-1}$) and 4 ($U_D = 8\,\mathrm{cm\,min}^{-1}$) at depth z1. These reference cases have a constant dip of (a) 70° (Exp. 3) and (b) 30° (Exp. 4), respectively. The marker speed, u^* (c), trench-normal speed component, $u_\perp^*$ (d), trench-parallel speed component, $u_\|^*$ (e) and normalized approach angle [$A_{\mathrm{norm}} = A_W$ divided by 180° (=trench-normal)] (f) are shown for selected markers in Zones 1–4 (denoted by red and blue lines in a–b). Black lines with triangles show the location of the trench. The dotted line represents the slab centreline. Slab segment dip values are shown above their corresponding halves of the trench.
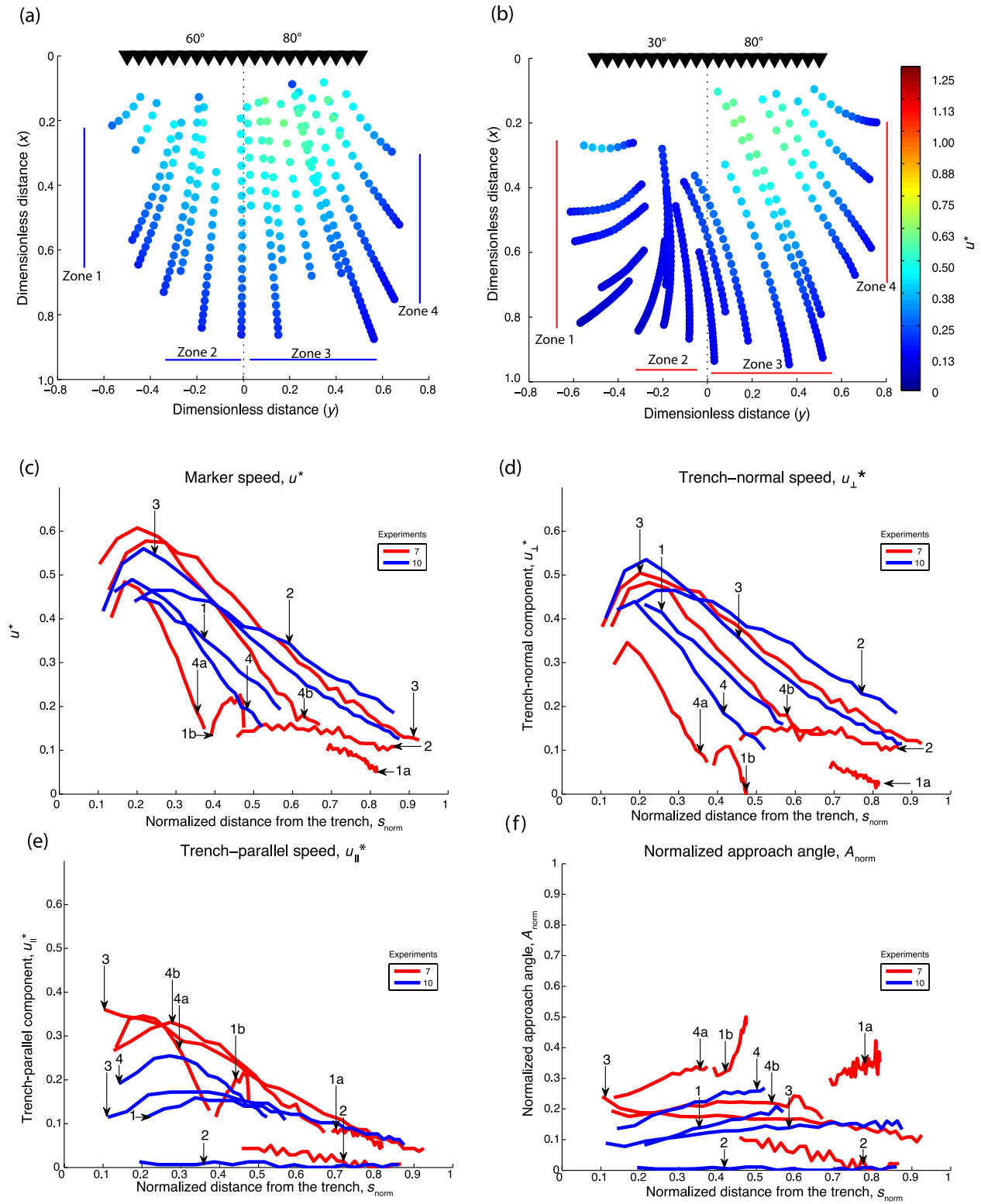
Figure A2. Comparison of Exps 10 ($U_D = 8$ cm min^{-1}) and 7 ($U_D = 8$ cm min^{-1}) at depth z1. Path line plots for (a) smallest gap width at the steepest possible dips (60°/80°, Exp. 10) and (b) the largest gap area (30°/80°, Exp. 7) are shown. The marker speed, u^* (c), trench-normal speed component, $u_\perp^*$ (d), trench-parallel speed component, $u_\parallel^*$ (e) and normalized approach angle (f) are shown for selected markers in Zones 1–4 (denoted by red and blue lines in a–b), where in some zones, multiple markers are plotted to display the full range of variety. Black lines with triangles show the location of the trench. The black dotted line represents the slab centreline. Slab segment dip values are shown above their corresponding halves of the trench.
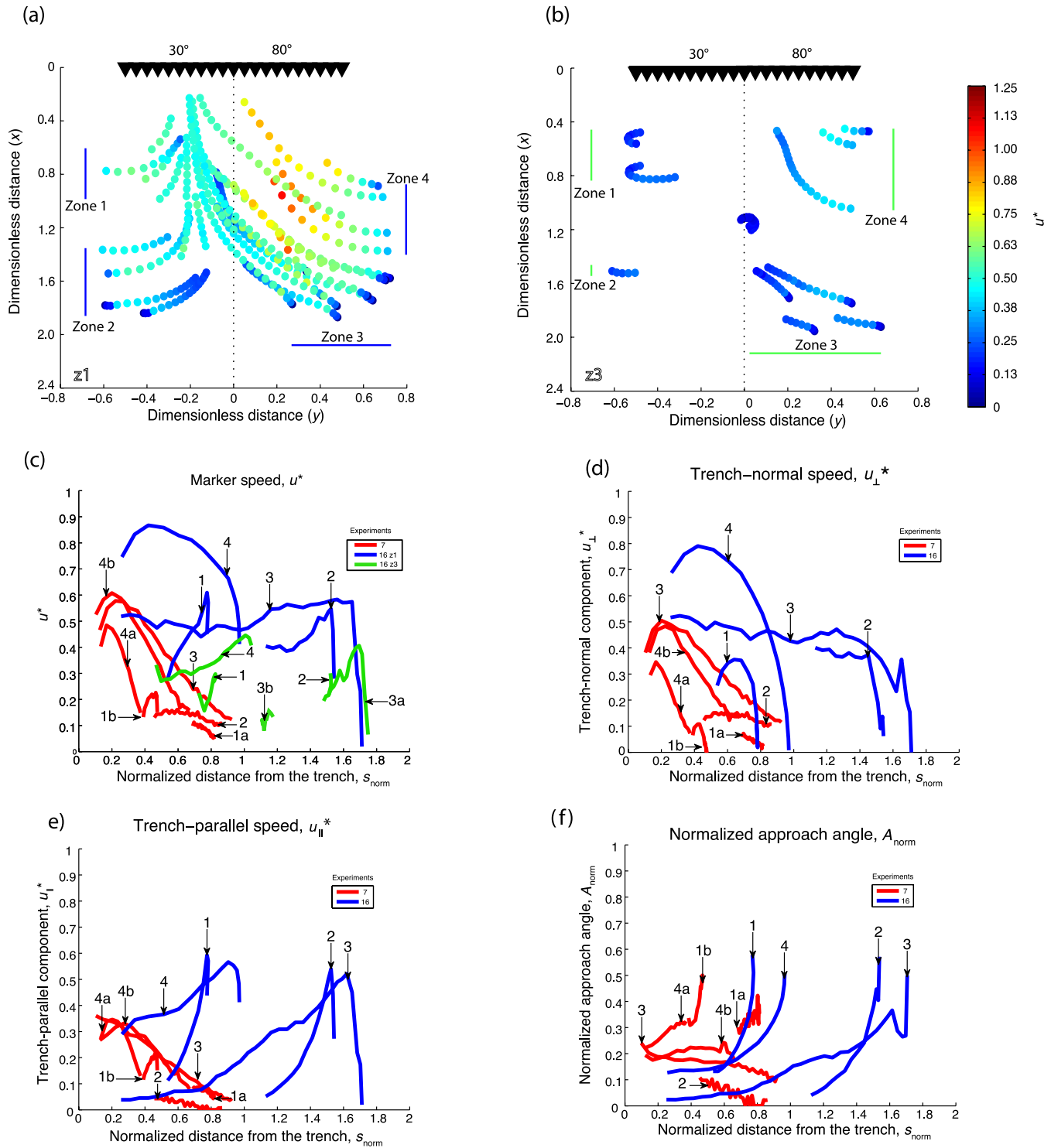
Figure A3. Comparison of Exp. 16 ($U_{\mathrm{D}} = 8\,\mathrm{cm\,min^{-1}}$, $U_{\mathrm{R}} = 3\,\mathrm{cm\,min^{-1}}$) at depths z1 and z3, with additional data from Exp. 7 ($U_{\mathrm{D}} = 8\,\mathrm{cm\,min^{-1}}$). The plots for an experiment with both the maximum slab gap size and rollback (Exp. 16) at depths of (a) z1 ($=2\,\mathrm{cm} \approx 100\,\mathrm{km}$) and (b) z3 ($=7\,\mathrm{cm} \approx 350\,\mathrm{km}$) are shown. The marker speed, u^* (c), trench-normal speed component, $u_\perp^*$ (d), trench-parallel speed component, $u_\parallel^*$ (e) and normalized approach angle (f) are shown for selected markers in Zones 1–4 (denoted by blue and green lines in a–b), where in some zones, multiple markers are plotted to display the full range of marker characteristics within that zone. The conditions contrasted in (c–f) are those of the maximum slab gap size without (Exp. 7) and with (Exp. 16) rollback. Red and blue lines are for the z1 plane comparison of Exp. 16 (Fig. A3a) and Exp. 7 (Fig. A2b), but green lines in (c) correspond to the z3 plane of Exp. 16 (Fig. A3b). Black lines with triangles show the location of the trench. The dotted line represents the slab centreline. Slab segment dip values are shown above their corresponding halves of the trench.
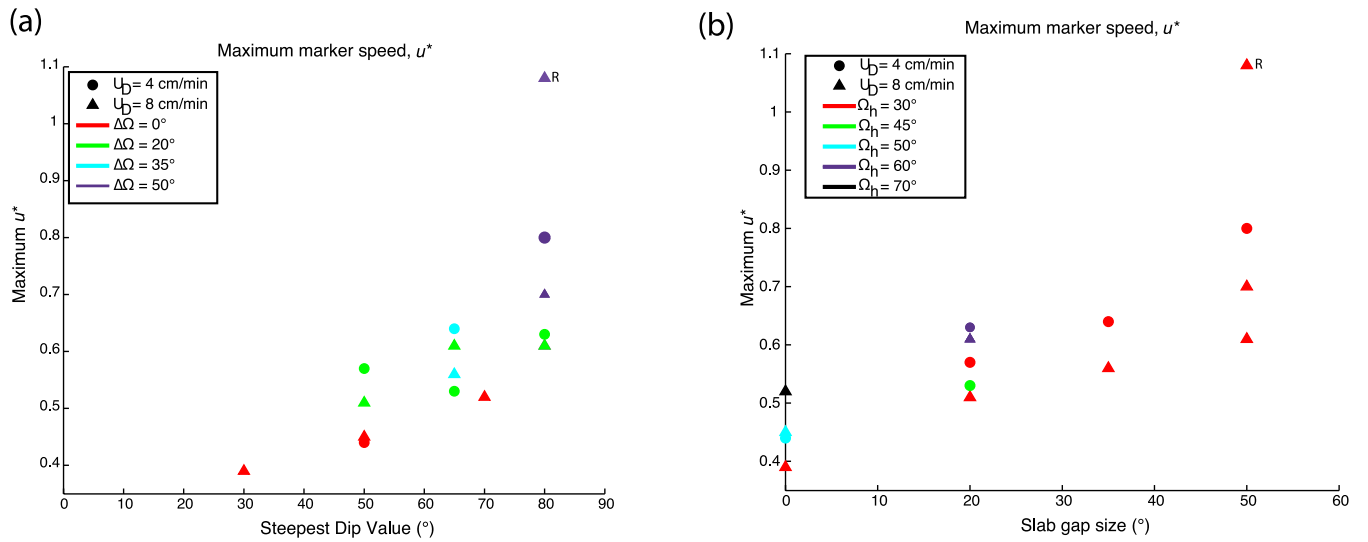
Figure A4. Summary of maximum marker speeds (u^*) plotted according to both slab gap size ($\Delta\Omega$) and steepest dip value. (a) Maximum marker speeds calculated over all paths for level z1 in each experiment, shown according to the steepest dip value in each experiment. (b) represents the same data as in part (a); we have changed the *x*-axis in this diagram to illustrate that the gap size, rather than the steepest dip value (a), drives the increase in u^*. $\Delta\Omega$ represents the slab gap size, and Ω_h represents the shallowest dipping slab in a given experiment. The 'R' in both (a) and (b) represents the values for Exp. 16, which is the only experiment where we added slab rollback.
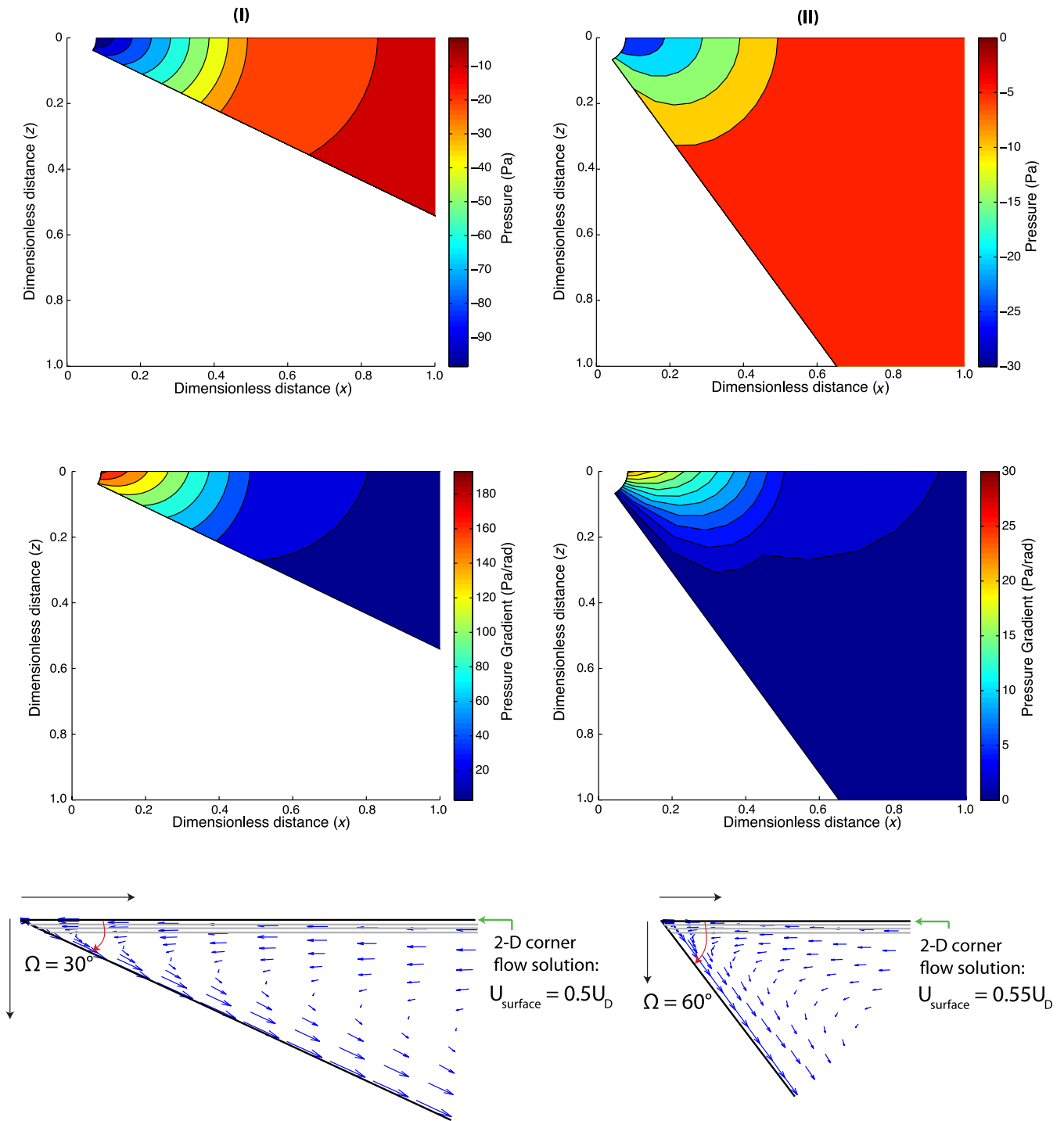
Figure A5. 2-D analytical corner flow solutions for the non-hydrostatic pressure (upper), pressure gradient (middle) and flow velocity (lower) values for (I) $\Omega = 30°$ and (II) $\Omega = 60°$. The grey lines in the flow field diagrams represent the depths at which our horizontal light sheets would fall on these slabs. Black arrows in the velocity plots correspond to the full extent of the vertical and horizontal axes displayed in the pressure and pressure gradient solutions. Distances are normalized by the total slab width ($W = 25$ cm). Note the different colour bar ranges.
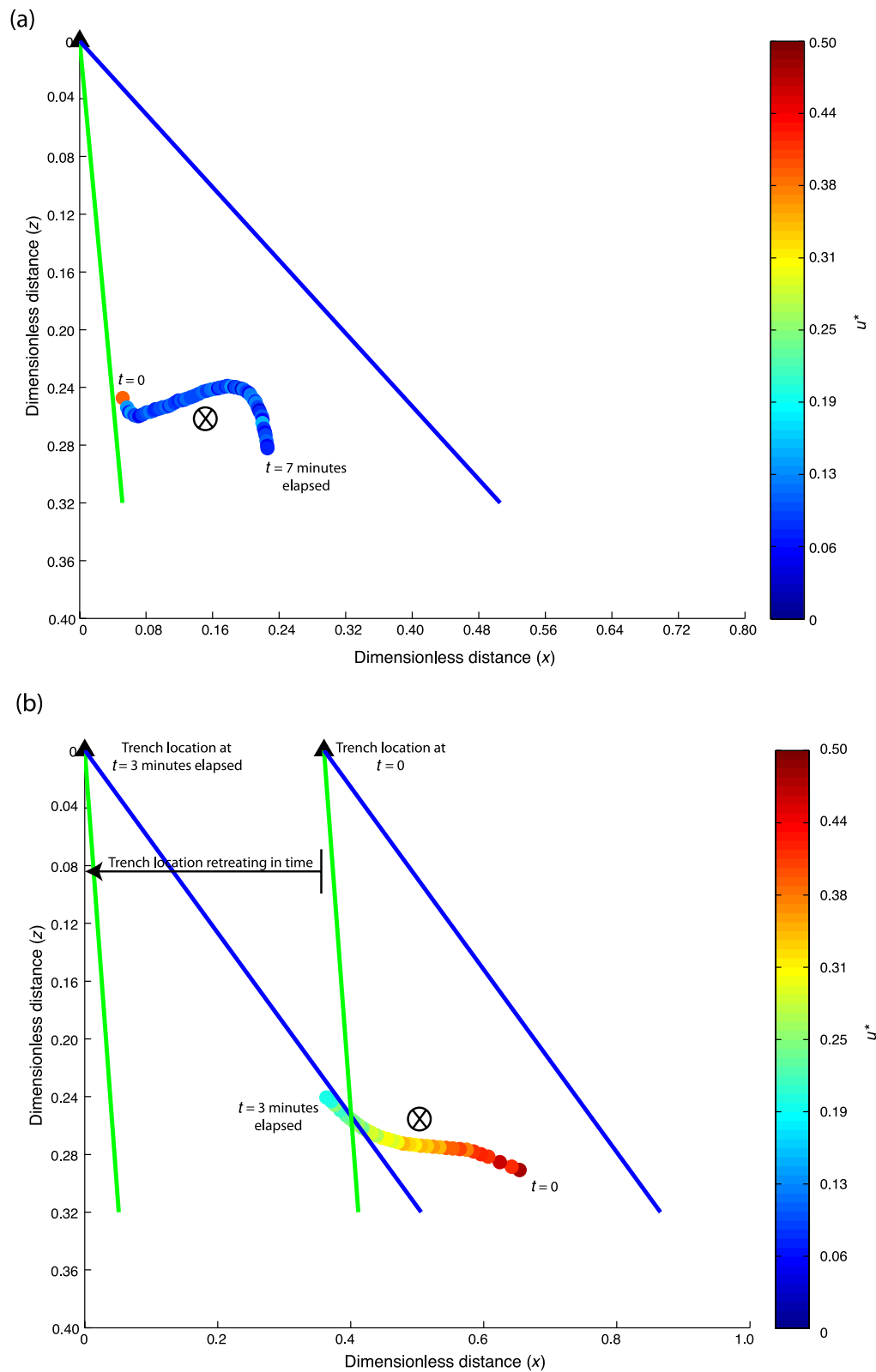
Figure A6. Marker paths over the given time intervals through the slab gap and into the mantle wedge for experiments with the maximum slab gap and subduction rate both (a) without (Exp. 7) and (b) with rollback (Exp. 16). Trench location is denoted by a black triangle, the steeply dipping slab is denoted by a green line and the shallowly dipping slab is denoted by a blue line. Time values show the evolution of the trench and bead location during rollback. The circular symbol with an 'x' in it denotes that the trench-parallel sense of motion is from beneath the shallowly dipping slab into the mantle wedge above the steeply dipping slab (i.e. into the page). Distances are normalized by the total slab width ($W = 25$ cm).

SUPPORTING INFORMATION

Additional Supporting Information may be found in the online version of this article:

Video S1. Map view of the uppermost light sheet (z1) of Experiment 4.
Video S2. Map view of the uppermost light sheet (z1) of Experiment 7.

Video S3. Map view of the uppermost light sheet (z1) of Experiment 16.
Table S1. This is the full data table over which the results in the table of Fig. 10 are averaged by backazimuth (http://gji.oxfordjournals. org/lookup/suppl/doi:10.1093/gji/ggu053/-/DC1)

Please note: Oxford University Press is not responsible for the content or functionality of any supporting materials supplied by the authors. Any queries (other than missing material) should be directed to the corresponding author for the article.